

# On the occurrence of a less usual rainfall pattern in northeastern Brazil during the 2019 El Niño

Victor Azevedo Godoi (✉ [victorgodoirj@gmail.com](mailto:victorgodoirj@gmail.com))

OceanPact Geo Ltd <https://orcid.org/0000-0001-7951-3017>

Felipe M. de Andrade

University of Reading - Whiteknights Campus: University of Reading

---

## Research Article

**Keywords:** Rainfall, northeastern Brazil, El Niño, anomalous heat sources, Madden–Julian Oscillation (MJO), linear baroclinic model

**Posted Date:** August 4th, 2021

**DOI:** <https://doi.org/10.21203/rs.3.rs-227770/v1>

**License:** © ⓘ This work is licensed under a Creative Commons Attribution 4.0 International License.

[Read Full License](#)

---

1 On the occurrence of a less usual rainfall pattern in northeastern Brazil during the 2019 El Niño

2

3 Victor A. Godoi<sup>1\*</sup>, Felipe M. de Andrade<sup>2</sup>

4 <sup>1</sup>OceanPact Geo Ltd – R. Paulo Emídio Barbosa, s/n, Quadra 6a, Módulo 6 – Technology Park, Federal  
5 University of Rio de Janeiro, Rio de Janeiro – RJ, 21941-615, Brazil.

6 <sup>2</sup>Department of Meteorology, Harry Pitt Building, University of Reading, Whiteknights Campus, Earley  
7 Gate, PO Box 243, Reading RG6 6BB, UK.

8 \*corresponding author: victorgodoirj@gmail.com; phone: +55 21 9 72321272; ORCID: 0000-0001-7951-  
9 3017

10 Second author's ORCID: 0000-0001-6653-3916

11

## 12 **Abstract**

13 El Niño is generally associated with below-average rainfall in northeastern Brazil (NEB). In 2019, however,  
14 the opposite rainfall pattern was observed during an El Niño episode. Here, we explore the mechanisms  
15 that overwhelmed typical El Niño-related conditions and resulted in above-average rainfall in NEB. We  
16 focus on the austral autumn, when El Niño is most related to rainfall anomalies in the region. The analysis  
17 of rainfall data from weather stations and the Global Precipitation Climatology Project, upper- and lower-  
18 level circulation reanalysis data, sea surface temperature data, outgoing longwave radiation data, and  
19 modelled data allowed us to identify that the autumn 2019 heavy rainfall in NEB was likely associated with  
20 three combined factors; these are: (1) the weak intensity of the 2019 El Niño; (2) local and remote diabatic  
21 heating anomalies, especially over the western South Pacific and tropical South Atlantic, which resulted in  
22 anticyclonic and cyclonic circulations in the upper and lower troposphere, respectively, over the tropical  
23 South Atlantic; and (3) sub-seasonal atmospheric convection anomalies over the western South Pacific,  
24 which reinforced the low-frequency convection signal over that region. This latter factor suggests the  
25 influence of the Madden–Julian Oscillation on rainfall in NEB during the first ten days of March. We discuss  
26 these mechanisms in detail and provide evidence for their associations with the anomalously heavy rainfall  
27 in NEB. Our results may assist in the planning of several crucial activities, such as water resources  
28 management and agriculture.

29

30 *Keywords:* Rainfall, northeastern Brazil, El Niño, anomalous heat sources, Madden–Julian Oscillation  
31 (MJO), linear baroclinic model.

32

## 33 **Declarations**

- 34 - Funding: No funding was received to assist with the preparation of this manuscript.  
35 - Conflicts of interest/Competing interests: The authors declare no conflicts of interest.  
36 - Availability of data and material: The data and material used in this research can be found at the  
37 following websites:

38 [www.inmet.gov.br](http://www.inmet.gov.br),  
39 <https://apps.ecmwf.int/datasets/data/interim-full-moda/levtype=sfc/>,  
40 <https://psl.noaa.gov/data/gridded/data.noaa.ersst.v5.html>,  
41 [https://psl.noaa.gov/data/gridded/data.interp\\_OLR.html](https://psl.noaa.gov/data/gridded/data.interp_OLR.html),  
42 <https://psl.noaa.gov/data/gridded/data.gpcp.html>,  
43 <https://ccsr.aori.u-tokyo.ac.jp/~lbn/sub/lbn.html>  
44 - Code availability (software application or custom code): The codes used in this research are  
45 available under request to the first author.  
46 - Authors' contributions: Both authors contributed to the study conception and design, material  
47 preparation, data analysis, and writing of this manuscript.

48  
49  
50  
51  
52  
53  
54  
55  
56  
57  
58  
59  
60  
61  
62  
63  
64  
65  
66  
67  
68  
69  
70  
71

## 72 **1. Introduction**

73 Accurate rainfall predictions are of paramount importance to water resources management,  
74 agriculture, livestock, energy generation (in those countries where hydropower has been adopted), and the

75 safety of people and infrastructure. To predict rainfall accurately, knowledge of its local and remote drivers  
76 is essential.

77         Rainfall can be associated with phenomena varying in a wide range of timescales, from a  
78 cumulonimbus cloud, which can develop and dissipate in less than an hour (Wallace et al. 2006; Houze  
79 2014), to persistent disturbances related to low-frequency climate oscillations, whose phases can last up  
80 to decades (e.g., Pacific Decadal Oscillation – Mantua and Hare 2002). A climate oscillation that has long  
81 attracted considerable attention from both the scientific community and industry is El Niño–Southern  
82 Oscillation (ENSO – Walker and Bliss 1932, 1937; Bjerknes 1961, 1966; Wyrski 1975; Neelin et al. 1998).  
83 ENSO is an interannual oscillation (2–7 years – Trenberth and Hurrell 1994; Cane 2005; McPhaden et al.  
84 2006) composed of two active phases, El Niño and La Niña, whose main signatures are observed through  
85 sea surface temperature (SST) variations in the central and eastern equatorial Pacific waters (Chase et al.  
86 2006). El Niño is associated with anomalously warm waters, and La Niña with anomalously cold waters.

87         ENSO has been related to rainfall anomalies all over the globe (Lin and Qian 2019). For example,  
88 southeastern Australia can experience severe droughts during El Niños (Nicholls 1985, 1991; Cai and  
89 Cowan 2008; Taschetto and England 2009; Cai et al. 2011; Davey et al. 2014), while heavy rainfall generally  
90 occurs in Peru and southern Brazil (Davey et al. 2014; Cai et al. 2020). ENSO-related SST variations in the  
91 central and eastern Pacific influence weather in remote locations through teleconnection mechanisms.  
92 Moisture, momentum, and heat transports from a tropical area to another are carried out by the Walker  
93 circulation (tropic-tropic teleconnection), and from a tropical to a subtropical area by the Hadley circulation  
94 (Grimm and Ambrizzi 2009; Stan et al. 2017). Variations in the Hadley cell, resulting from tropical diabatic  
95 (convective) heating anomalies, disturb subtropical Rossby wave sources (Shimizu and Cavalcanti 2011),  
96 which, in turn, induce barotropic Rossby waves that change the flow at mid and high latitudes (L'Heureux  
97 and Thompson 2006) (tropical-extratropical teleconnection).

98         Northeastern Brazil (NEB) is one of the regions impacted by ENSO fluctuations (Grimm 2011;  
99 Tedeschi et al. 2015, 2016), with severe droughts generally occurring during El Niños (Rodrigues et al.  
100 2011), and heavy rainfall during La Niñas (Rodrigues and McPhaden 2014). The strength of rainfall  
101 anomalies in NEB may change according to the ENSO flavour and year's season. Moderate rainfall  
102 anomalies are associated with central Pacific (Modoki) El Niño events, whereas stronger anomalies relate  
103 to eastern Pacific (canonical) El Niño events (Rodrigues et al. 2011). On the other hand, rainfall anomalies  
104 in NEB are generally strong during both central and eastern Pacific La Niña events (Tedeschi et al. 2016).  
105 Rainfall extremes are most pronounced in the austral autumn (Grimm 2011), when rainfall anomalies can  
106 have opposite signals during the different ENSO flavours – below-average rainfall is usually expected  
107 during canonical El Niños, while above-average rainfall can occasionally occur during El Niño Modoki  
108 (Tedeschi et al. 2016). Despite these relationships between ENSO events and rainfall in NEB being  
109 relatively well established, no two El Niño/La Niña episodes have exactly the same characteristics (Cai et  
110 al. 2020). The mechanisms responsible for different rainfall conditions between events need to be well  
111 understood, especially those that result in anomalies whose sign is contrary to that expected for a given

112 ENSO phase (as in Grimm et al. 2020). Sectors requiring rainfall information to plan their activities will  
113 benefit greatly from this knowledge.

114         Although rainfall anomalies in NEB are generally negative (below-average rainfall) during El Niño  
115 episodes, the opposite rainfall pattern was observed in the austral autumn [March–April–May (MAM) –  
116 herein, we use the acronym “MAM” to refer to austral autumn in a general sense, not necessarily from  
117 beginning to end of the season] during the 2019 El Niño – this rainfall behaviour is shown and discussed in  
118 detail in Section 4. Seasonal forecasts issued in February 2019 already indicated a 35–40% chance of  
119 unusually wet conditions in NEB for MAM (Nobre et al. 2019). Such unusual 2019 wet conditions have not  
120 yet been explored. Here, we investigated the dynamical processes related to this atypical rainfall behaviour  
121 in NEB during the 2019 El Niño by analysing several datasets. Firstly, we examined upper- and lower-level  
122 circulation reanalysis data, SST data, and gridded rainfall data to understand the atmospheric and oceanic  
123 conditions that prevailed during the period of analysis and those that are generally observed during El Niño  
124 episodes. Secondly, we used weather station rainfall data to analyse the most intense rainfall anomalies in  
125 NEB in MAM 2019. Thirdly, the regions where anomalous heat sources (diabatic heating anomalies) could  
126 have brought about the circulation anomalies that resulted in rainfall in NEB were inferred from rainfall data  
127 and by applying the influence functions (IFs) approach to the results of a dry linear baroclinic model (LBM).  
128 The same model was then run to investigate how these diabatic heating anomalies could potentially have  
129 modulated above-normal rainfall in NEB in March 2019. The simulations focussed on March 2019 because  
130 this was the month when rainfall anomalies were most extreme and the Madden–Julian Oscillation (MJO –  
131 Madden and Julian 1971, 1972, 1994) phase was favourable to rainfall in NEB (shown later). Recent work  
132 has demonstrated that the MJO is associated with rainfall in NEB (e.g., Grimm 2019; Giovannetone et al.  
133 2020). The MJO is the dominant mode of sub-seasonal variability in the tropical atmosphere (Mo and  
134 Nogues-Paegle 2005), and can modulate ENSO-related impacts over South America (Shimizu and  
135 Ambrizzi 2016; Shimizu et al. 2017). Since rainfall conditions in NEB during the 2019 austral autumn  
136 differed from those expected during El Niño episodes, we also looked into how MJO activity could have  
137 contributed to circulation anomalies associated with these conditions. This was carried out by using the  
138 daily Real-time Multivariate MJO (RMM) index (Wheeler and Hendon 2004) and filtered outgoing longwave  
139 radiation (OLR – as a proxy for tropical deep atmospheric convection) fields.

140         The datasets and model simulations mentioned in the previous paragraph are described in the next  
141 section, along with the methods employed in this work. Section 3 provides an overview of the typical  
142 behaviours of SST, rainfall, and upper- and lower-level circulations in MAM during El Niño events. Our  
143 results are presented and discussed in Sections 4–6. Lastly, our key findings are reported in Section 7.

144

145

## 146 **2. Data and methods**

147

148 Assessments of the upper- and lower-level atmospheric circulations, SST, and rainfall were made  
149 through 200-hPa and 850-hPa zonally asymmetric streamfunction (ZASTRF), SST, and rainfall fields,  
150 respectively. ZASTRF data were calculated from 200-hPa and 850-hPa zonal and meridional wind data  
151 sourced from the European Centre for Medium-Range Weather Forecasts (ECMWF) ERA-Interim  
152 reanalysis (Dee et al. 2011) at the spatial resolution of  $1.5^\circ \times 1.5^\circ$ . SST data were obtained from the National  
153 Oceanic and Atmospheric Administration (NOAA) Extended Reconstructed SST version 5 (ERSSTv5) at  
154 the  $2.0^\circ \times 2.0^\circ$  spatial resolution (Huang et al. 2017). Gridded rainfall data were sourced from the NOAA  
155 Global Precipitation Climatology Project (GPCP) at the spatial resolution of  $2.5^\circ \times 2.5^\circ$  (Adler et al. 2018).  
156 All data described in this paragraph are monthly and span March–May seasons between 1979 and 2019.  
157 Daily OLR data were also obtained to examine potential relationships between MJO convective activity and  
158 atmospheric circulation anomalies associated with the above-normal rainfall in NEB. OLR data were derived  
159 from the NOAA Interpolated OLR at the spatial resolution of  $2.5^\circ \times 2.5^\circ$  (Liebmann and Smith 1996). The  
160 spatial resolutions of ZASTRF and SST data were reduced to  $2.5^\circ \times 2.5^\circ$ , using linear interpolation, to  
161 facilitate the comparison to the results generated here and to obtain a uniform resolution among the  
162 ZASTRF, SST, rainfall, and OLR data. ZASTRF, SST, rainfall, and OLR anomalies were calculated using  
163 the 1979–2019 long-term mean.

164 Monthly accumulated rainfall data, measured at seven weather stations near the northern coast of  
165 NEB (Fig. 1), were sourced from the Brazilian National Institute of Meteorology (INMET). The selection of  
166 stations was based on location and data availability. We focussed on stations near the coastline sector  
167 between northwestern Maranhão (MA) and northeastern Rio Grande do Norte (RN) whose data span the  
168 period March 1979–May 2019. As we show later, this coastline sector experienced the highest rainfall  
169 amounts in NEB in MAM 2019. To determine the strength of rainfall anomalies in MAM 2019 and the months  
170 within that season, seasonal and monthly anomalies were normalised by the standard deviation.  
171 Calculations considered the period 1979–2019 as the climatological reference. Seasonal anomalies were  
172 computed only for years whose March, April, and May data were available. Extreme positive [negative]  
173 anomalies were defined as those values higher [lower] than one standard deviation about the mean.

174 To provide an overview of the SST, rainfall, and upper- and lower-level circulations typical  
175 behaviours in MAM during El Niño events, we calculated least-squares linear regressions of SST, rainfall,  
176 and ZASTRF seasonal anomalies onto ENSO indices. Niño 3, Niño 4, and Niño 3.4 indices were calculated  
177 by averaging SST anomalies over their respective regions (Trenberth 1997; Trenberth and Stepaniak  
178 2001). The indices were, then, normalised by their respective standard deviations. The calculation of the El  
179 Niño Modoki Index (EMI; Ashok et al. 2007) followed standard procedures. Regression calculations  
180 considered the period 1979–2019. SST, rainfall, and ZASTRF fields were scaled by one standard deviation  
181 anomaly of the ENSO indices, following Lo and Hendon (2000). Statistical significance of regressed values  
182 was evaluated using a two-tailed Student's *t*-test (Allen 1997) and a confidence level equal to 90% (*p*-value  
183 equal to 0.1). This test considered the effective number of spatial degrees of freedom described in Livezey

184 and Chen (1983). As the regressed fields onto Niño 3, Niño 4, and Niño 3.4 indices are roughly similar (not  
185 shown), we only show and discuss regression results for Niño 3.4 and EMI.

186 We conducted two sets of numerical simulations to achieve two different goals: (1) to identify the  
187 diabatic heating anomalies that most disturbed the circulation at a few target locations. To accomplish that,  
188 we used a dry LBM – i.e., with no moisture effects – and the IFs approach. IFs have been generally applied  
189 to the results of barotropic vorticity equation models to assess the impacts of vorticity and divergence  
190 sources on atmospheric circulation, and are an invaluable tool to diagnose the origin of tropical-extratropical  
191 teleconnections (e.g., Branstator 1985; Grimm and Silva Dias 1995; Grimm 2003; Grimm and Reason 2011,  
192 2015; Grimm 2019); and (2) to confirm the origin of the atmospheric circulation anomalies that most  
193 contributed to the occurrence of above-normal rainfall in NEB in March 2019. The dry LBM used to achieve  
194 goal number (1) was also employed to achieve goal number (2).

195 We chose the dry LBM described in Watanabe and Kimoto (2000) to carry out the simulations, and  
196 this was because this model easily allows for the separation of anomalous atmospheric responses from the  
197 basic state (Tseng et al. 2019). LBMs include the effect of mean zonal wind vertical shear, which plays a  
198 crucial role in the meridional propagation of planetary-scale circulation anomalies triggered by tropical heat  
199 sources (Kasahara and Silva Dias 1986; Majda and Biello 2003).

200 The simulations used thermal forcings (TFs) in the model's temperature tendency equation, and  
201 the March climatology (1979–2019) to integrate the primitive equations. The climatological basic state was  
202 composed of temperature and wind fields at 23 pressure levels (allocated between 1000 hPa and 1 hPa)  
203 and surface pressure, all extracted from the ECMWF ERA-Interim reanalysis. These data were interpolated,  
204 at 20 sigma levels (L20), to the coarsest model resolution (i.e.,  $5.625^\circ$  – triangular spectral truncation at  
205 zonal wavenumber 21 – T21) to reduce computational costs. Sensitivity tests considering the finer spatial  
206 resolution T42 were also carried out. Although T42 resolution is generally adequate for representing most  
207 quantities of interest in climate diagnostics (Trenberth and Solomon 1993), results did not improve  
208 significantly (not shown). To enhance stability and inhibit the development of small-scale eddies, Rayleigh  
209 friction and Newtonian cooling were considered in the simulations using an e-folding timescale of 20 days  
210 in all vertical layers, except at the topmost sigma level and the lowest three levels, where the damping  
211 timescale was defined as 0.5 days, following Tseng et al. (2020). A sixth-order biharmonic horizontal  
212 diffusion ( $\nabla^6$ ), with damping timescale of 20 hours for the shortest wavelength (Jin and Hoskins 1995;  
213 Ambrizzi and Hoskins 1997), was also employed.

214 The model was integrated for 30 days, considering a 40-minute timestep and a steady TF. The  
215 *quasi*-stationary circulation response to anomalous diabatic heating occurred around the fifteenth day of  
216 the simulations (before baroclinic instability dominated the flow), which corroborates the results of previous  
217 work (e.g., Jin and Hoskins 1995; Seo and Son 2012). Thus, our discussions on the modelled results  
218 concern day 15 of the simulations. Modelled 200-hPa and 850-hPa streamfunction fields had their zonal  
219 mean removed, hence becoming ZASTRF fields, to make teleconnection responses more notable (e.g., Jin  
220 and Hoskins 1995; Grimm and Reason 2011, 2015).



258 comprises different physical processes, such as condensation heating, evaporation, radiative cooling, and  
259 eddy heat flux convergence (Yanai et al. 1973), condensation heating dominates in regions of deep  
260 convective activity. The calculation of  $Q_1$  anomalies for March 2019 considered the period 1979–2019 as  
261 the climatological reference.

262 Lastly, as we show in Section 4, accumulated rainfall varied considerably from month to month in  
263 MAM 2019, suggesting that sub-seasonal atmospheric variability might have contributed to modulating  
264 rainfall anomalies. To point out potential links between the MJO and rainfall anomalies in NEB, we used  
265 the RMM index. A more thorough exam of such links was carried out by filtering daily OLR anomalies for  
266 March 2019 at low frequency (>90 days) and the sub-seasonal band (30–90 days) using a Lanczos filter  
267 (Duchon 1979) – we focussed on March 2019 because that is when MJO phases seem to have favoured  
268 rainfall intensification in the study area the most (shown later). Filtered OLR anomalies were monthly  
269 averaged for each frequency band, and the resulting averages were compared between themselves and  
270 to the unfiltered monthly anomaly for March 2019.

271

272

### 273 **3. Overview of El Niño-related conditions in the austral autumn**

274 To facilitate our discussions, we describe very briefly, in this section, SST, rainfall, and upper- and  
275 lower-level circulation conditions associated with El Niño events in the austral autumn. The description is  
276 based on linear regressions of SST, rainfall, and ZASTRF onto two ENSO indices, the Niño 3.4 and EMI.

277 Temporary changes to tropical SST typical patterns, like those that happen during El Niño events,  
278 generally induce variations in both intensity and location of tropical atmospheric convection. These  
279 variations, in turn, generate atmospheric circulation anomalies that influence weather and climate all over  
280 the globe (Trenberth and Caron 2000). SST anomalies in the tropical Pacific strongly influence rainfall  
281 conditions in NEB. Fig. 2 shows that anomalous warming (positive SST anomalies) in the central and  
282 eastern tropical Pacific (Niño 3.4 region – 5°S–5°N, 170°–120°W) usually results in increased rainfall in  
283 those regions, and reduced rainfall in NEB. Also related to this anomalous warming are the upper-level  
284 cyclonic and lower-level anticyclonic circulations over NEB (positive and negative ZASTRF anomalies,  
285 respectively), which are associated with decreases in rainfall in NEB and, on some occasions, severe  
286 droughts (Cai et al. 2020) – the opposite circulation pattern appears over the central and eastern tropical  
287 Pacific. On the other hand, Fig. 3 shows that warmer SST centred at about 0° × 180°, associated with El  
288 Niño Modoki events, generally induces increased rainfall right over it and to the west of it, and reduced  
289 rainfall along the tropical Pacific, from about 170°W all the way to South America. Reduced rainfall is also  
290 observed over most parts of NEB, although with no statistical significance (other studies, e.g., Cai et al.  
291 (2020), have found statistically significant results when relating El Niño Modoki events to rainfall in NEB,  
292 which may result from the period of analysis and technique employed by the authors). Upper- and lower-  
293 level circulation patterns are similar to those shown in Fig. 2, but less intense and shifted westward. The  
294 lower-troposphere circulation over NEB, however, is not statistically significant in Fig. 3. Therefore,

295 circulation patterns related to both canonical and Modoki events induce decreases in rainfall in NEB, which  
296 are more remarkable close to the northern coast, as also shown in Cai et al. (2020). Despite that, the  
297 intensity and statistical significance of El Niño Modoki-related atmospheric conditions over NEB indicate  
298 that rainfall anomalies are more likely to deviate from the expected behaviour than those related to  
299 canonical El Niños (also shown in Tedeschi et al. 2016).

300

301

## 302 **4. Oceanic and atmospheric conditions in the 2019 austral autumn**

### 303 *4.1 SST and rainfall anomalies*

304 In MAM 2019 and the months within that season, El Niño-related warmest waters occurred in the  
305 central Pacific, centred at around 165°W (see SST fields in Fig. 4). Heavier rainfall was also observed in  
306 the central Pacific (Fig. 4), with the highest amounts taking place further to the west, at around the  
307 International Date Line (180°). In March 2019, heavier rainfall and warmer SST occurred in the tropical  
308 South Atlantic and near the southeastern coast of Australia, in the Tasman Sea, whereas the tropical  
309 western South Pacific experienced lighter (below-normal) rainfall (the importance of these regions to our  
310 study is evidenced later).

311 Heavier-than-usual rainfall has been found to take place in NEB when waters in the Niño 3.4 region  
312 are warmer than 0.5°C and deep convection is absent over these waters, as occurred at the initial stages  
313 of the 2018–2019 El Niño – this rainfall pattern is, nevertheless, statistically non-significant (Hu et al. 2020).  
314 If deep convection is present over the Niño 3.4 region warmer waters instead, rainfall in NEB is significantly  
315 lighter than usual (Hu et al. 2020 – we note that this comment and the previous one are based on  
316 composites of monthly mean precipitation anomalies for the period January 1979–December 2019).  
317 Despite SST and rainfall conditions in the Niño 3.4 region in MAM 2019 resembling this second case more  
318 (deep convection failed to exist everywhere over the Niño 3.4 region, though – not shown), rainfall was  
319 anomalously heavy in most parts of NEB (Fig. 4).

320 Rainfall fields show that the highest rainfall amounts in NEB in MAM 2019 occurred in the region's  
321 northern portion (Fig. 4). Because of that, we expand our discussion considering weather station rainfall  
322 data measured at seven sites near the NEB northern coastline sector (Fig. 1). Furthermore, to understand  
323 the relative strength of the rainfall anomalies observed in MAM 2019, we compare them to those observed  
324 during three extreme El Niños. These extreme events supposedly reveal the relationship between El Niños  
325 and their associated rainfall anomalies in NEB more clearly than non-extreme events and, therefore,  
326 provide the reader with a better understanding of such a relationship.

327 The usual rainfall behaviour in NEB during El Niño events can be clearly noted in some time series  
328 of Fig. 5 in years of extreme El Niños, such as 1983, 1998, and 2016 (vertical dotted lines). Drought (i.e.,  
329 normalised anomaly values lower than -1 standard deviation) for the following stations reflects the 1983 El  
330 Niño intensity: Turiaçu and São Luís (March, April, and May), Piri-piri (April), Sobral (March and April), and  
331 Fortaleza (April and May). These outstandingly small rainfall amounts can also be noted for all stations in

332 MAM 1983, except for Apodi and Ceará-Mirim. In 1998, drought in NEB was less severe than in 1983, in  
333 general. In other words, normalised anomaly values for 1998 were higher than those observed in 1983 at  
334 most stations and in most periods (months and season) analysed. The easternmost stations (Apodi and  
335 Ceará-Mirim) are exceptions. At Apodi station, negative rainfall anomalies were more pronounced in April,  
336 May, and MAM 1998 than in the same period in 1983; although in MAM, normalised anomalies were  
337 extreme in neither 1983 nor 1998. Rainfall at Ceará-Mirim station behaved similarly, with negative  
338 normalised anomalies more pronounced in March, April, and MAM 1998. In this case, however, anomalies  
339 were not extreme in April of both years. A multi-year drought in NEB started in 2011 (Grimm 2018), and  
340 was aggravated by the 2016 El Niño-related effects. Such drought affected over 30 million people and  
341 resulted in more than US\$25 billion in economic losses (Cai et al. 2020). The weather stations' data selected  
342 here show that the 2016 extreme El Niño was the least associated with drought in the northernmost portion  
343 of NEB, compared to both 1983 and 1998 events. Normalised anomalies for 2016 were extremely negative  
344 only at Turiaçu (May), Piripiri (April), and Apodi (April and MAM). The 2016 extreme values were lower than  
345 those of 1983 (April and MAM) and 1998 (MAM) only at Apodi station, which may be associated, for  
346 instance, with local effects, or even the Atlantic Multidecadal Oscillation phase change around 1998  
347 (Kayano and Capistrano 2014; Levine et al. 2017). A remarkable difference among these three El Niño  
348 events is their signature in the Pacific Ocean. Above-average SST featured most prominently in eastern  
349 equatorial Pacific waters during the 1983 and 1998 events, and in the western and central Pacific during  
350 the 2016 El Niño (L'Heureux et al. 2017).

351 The 2018–2019 El Niño was only weak (weaker east-west SST anomaly gradient across the  
352 tropical Pacific than usual El Niños – Hu et al. (2020)) and characterised by a delayed ocean-atmosphere  
353 coupling (Johnson et al. 2019) – i.e., tropical deep atmospheric convection did not shift eastward at the El  
354 Niño initial stages despite conducive oceanic conditions. An anomalous SST gradient between the western  
355 and central equatorial Pacific delayed the formation of deep atmospheric convection over the central  
356 tropical Pacific and, consequently, of its associated teleconnection patterns (Johnson et al. 2019). Even  
357 though such initial decoupling only lasted from October to December 2018 (Hu et al. 2020), NEB  
358 experienced positive rainfall anomalies in MAM 2019 (Figs. 4 and 5), which contrasts the dry conditions  
359 typically observed in the region during El Niño episodes (Figs. 2 and 3). Positive rainfall anomalies were  
360 observed at all seven stations in March 2019, with extreme values occurring at four of them (Turiaçu, São  
361 Luís, Piripiri, and Ceará-Mirim). In April 2019, extreme rainfall took place at three out of the seven stations  
362 analysed (Turiaçu, Piripiri, and Ceará-Mirim). Fortaleza was the only station that experienced extreme  
363 rainfall in May 2019. In MAM 2019, positive anomalies were remarkably strong at three stations (Turiaçu,  
364 Piripiri, and Ceará-Mirim). Values were quite close to one standard deviation at all stations whose  
365 anomalies were not extreme in that season, excepting at Apodi station, where the normalised anomaly  
366 value was close to zero. It is worth noting that the three stations that experienced unusually heavy rainfall  
367 in MAM 2019 are not close together. In fact, two of these stations are the westernmost and easternmost

368 stations, whereas the third one is nearly in the middle of them. There were no extremely negative anomalies  
369 (below-normal rainfall) in the 2019 period analysed.

370 In 2019, São Luís, Ceará-Mirim, and Piripiri stations recorded not only high accumulated rainfall  
371 values but some of the highest values of the last 40 years (Fig. 5). At São Luís station, rainfall in March  
372 2019 was the heaviest on record (1979–2019) for March months, with the normalised anomaly value  $\sim 2.3$   
373 times higher than the standard deviation. Also in March 2019, Ceará-Mirim station experienced the third-  
374 heaviest March rainfall since 1979 ( $\sim 1.5$  heavier than the standard deviation). Moreover, rainfall amounts  
375 at Ceará-Mirim station in April and MAM 2019 were the second-heaviest relative to corresponding periods  
376 in previous years ( $\sim 1.9$  heavier than the standard deviation in both cases). In 2019, Piripiri station recorded  
377 the second- and third-heaviest rainfall amounts for April and MAM, respectively, when considering the  
378 period 1979–2019 ( $\sim 1.6$  and  $\sim 1.3$  heavier than the standard deviations for April and MAM, respectively).

379 The previous three paragraphs highlight the month-to-month rainfall amount differences for data  
380 recorded at individual weather stations during an El Niño event. These results for the austral autumn extend  
381 those found by Grimm (2003) for the extended austral summer (November–February). The aforementioned  
382 month-to-month differences suggest a contribution of sub-seasonal oscillations (e.g., the MJO) to rainfall  
383 variability in NEB, which can disturb El Niño-related impacts (addressed later in Section 6).

384

#### 385 *4.2 Atmospheric circulation anomalies*

386

387 The ocean-atmosphere coupling during MAM 2019 triggered circulation conditions over NEB (Fig.  
388 6) that differ from those expected during El Niño events (Figs 2 and 3). An upper-level (200 hPa) Rossby  
389 wave train connected the South Pacific to the tropical South Atlantic through the extratropics (more notable  
390 in MAM and March 2019), resulting in an anticyclonic circulation over the tropical South Atlantic and part of  
391 eastern South America (Fig. 6). This anticyclonic circulation likely caused upper-level divergence over NEB,  
392 favouring rainfall occurrence in the region, unlike the typically-observed dry conditions associated with El  
393 Niño-related cyclonic circulations (Figs 2 and 3). In the lower troposphere (850 hPa), the circulation also  
394 opposed the El Niño-related usual conditions, with a cyclonic circulation appearing over part of NEB, except  
395 in May 2019 (Fig. 6).

396

397

### 398 **5. Model results**

399 *5.1 Influence functions* The impacts of diabatic heating anomalies on circulation were assessed  
400 at five TPs (Fig. 7 – the TPs can also be seen in the March panels of Fig. 6). The selection of TPs 1–4  
401 aimed to understand the origin of the teleconnection pattern that connected the extratropical South Pacific  
402 to the tropical South Atlantic. TP5 was selected to identify potential TFs influencing the local circulation.

403 The IFs results for TPs 1–4 (Fig. 7) indicate that circulation anomalies associated with the  
404 teleconnection pattern observed in the reanalysis data (Fig. 6 – March panels) were likely triggered by TFs

405 over the western South Pacific – this is shown by the sign reversal of IF results as TP locations vary (Fig.  
406 7). Although TFs over other regions (e.g., central South Pacific) may seem to influence circulation around  
407 TPs strongly, the signs of IFs results do not reverse as TP locations change. The absence of such a sign  
408 reversal results in conflicting influences at the TPs, as highlighted by Grimm and Silva Dias (1995). The IFs  
409 results for TPs 1 and 2 show that the dipole-like rainfall pattern observed in the GPCP data, with negative  
410 anomalies (cooling) at  $\sim 12^{\circ}\text{S}/160^{\circ}\text{E}$  and positive anomalies (heating) at  $\sim 35^{\circ}\text{S}/160^{\circ}\text{E}$  (Fig. 4 – March  
411 panel), may trigger a barotropic circulation around these TPs (Fig. 7), like the one observed in the reanalysis  
412 data (Fig. 6 – March panels). TFs over the western South Pacific, especially near the eastern/southeastern  
413 coast of Australia (over the Tasman Sea), may also modulate circulation anomalies around TP3. IFs upper-  
414 and lower-level circulations show opposite signs over the western subtropical South Pacific (Fig. 7),  
415 indicating that the “*quasi*-baroclinic” circulation around TP3 (Fig. 6 – March panels) was likely induced by  
416 heating anomalies over the Tasman Sea (see March rainfall field in Fig. 4). To obtain the 200-hPa  
417 anticyclonic circulation and 850-hPa cyclonic circulation around TP4, as observed in Fig. 6 (March panels),  
418 the IFs results point out that cooling anomalies over most parts of the Pacific Ocean and Australia are  
419 necessary. Because IFs circulation anomalies over the western South Pacific all have signs of the same  
420 polarity for TP4, the effects of the dipole-like rainfall pattern on TP4 are likely smoothed. This is because  
421 the same sign polarity indicates conflicting influences, in this case, showing that the teleconnection pattern  
422 action centres around TPs 1–4 are not equally excited by the dipole-like rainfall pattern. The IFs results for  
423 TP4 also show that the local effects associated with heating anomalies over the tropical South Atlantic  
424 (March panel in Fig. 4) contribute to generating the baroclinic circulation observed in the reanalysis data  
425 (Fig. 6 – March panels). Regarding the effects of TFs on circulation around TP5, the IFs fields indicate that  
426 heating anomalies associated with heavy rainfall in the western-central equatorial Pacific likely modulate  
427 circulation anomalies over the region near the northern coast of NEB (Fig. 7). Local TFs associated with  
428 deep diabatic heating anomalies, on the other hand, do not seem to affect the local circulation. This is  
429 indicated by opposite 850-hPa and 200-hPa IFs circulation anomalies (baroclinic circulation) over the  
430 northern coast of NEB and adjacent equatorial Atlantic, which contrast those observed in reanalysis data  
431 (Fig. 6 – March panels).

432 The IFs results (Fig. 7), along with the GPCP rainfall data (Fig. 4 – March panel), suggest that deep  
433 diabatic heating anomalies (TFs) in four regions may have contributed the most to above-normal rainfall in  
434 NEB in March 2019. These regions comprise the following areas:  $\sim 5^{\circ}\text{S}–7.5^{\circ}\text{N} / 150^{\circ}\text{E}–170^{\circ}\text{W}$  (TF1);  
435  $\sim 20^{\circ}\text{S}–5^{\circ}\text{S} / 155^{\circ}\text{E}–170^{\circ}\text{E}$  (TF2);  $\sim 40^{\circ}\text{S}–25^{\circ}\text{S} / 152^{\circ}\text{E}–168^{\circ}\text{E}$  (TF3); and  $\sim 35^{\circ}\text{S}–15^{\circ}\text{S} / 43^{\circ}\text{W}–10^{\circ}\text{W}$  (TF4).  
436 The way this hypothesis was tested is explained next.

437

### 438 *5.2 Vertical and horizontal distributions of thermal forcings*

439 The vertical and horizontal distributions of TFs 1–4, incorporated into the model’s temperature  
440 tendency equation, are shown in Fig. 8. Their respective peaks are 13.1 K/day (at 500 hPa), -3.6 K/day (at  
441 400 hPa), 4.6 K/day (at 400 hPa), and 3.1 K/day (at 500 hPa). We considered, in addition, three forcing

442 nodes, two peaking in the lower troposphere (700 hPa and 850 hPa) and one in the upper troposphere (300  
443 hPa). One of the nodes peaking in the lower troposphere (-5.3 K/day at 700 hPa – TF5) relates to negative  
444 rainfall anomalies to the north of NEB; its associated area comprises ~2.5°S–7.5°N / 48°W–32°W (Fig. 8).  
445 The other one relates to positive rainfall anomalies over the entire equatorial Atlantic, and is associated  
446 with the Intertropical Convergence Zone (ITCZ) cloud band (not shown). The node peaking in the upper  
447 troposphere (300 hPa) relates to deep heating anomalies (heavy rainfall) over the northern coast of NEB  
448 (not shown). As shown later, the 850-hPa ZASTRF response over the tropical South Atlantic slightly  
449 improves when considering TF5. In contrast, the simulations that considered shallow heating anomalies  
450 over the entire equatorial Atlantic and deep heating anomalies over the northern coast of NEB did not  
451 provide additional insights into the modulation of atmospheric circulations associated with the above-normal  
452 rainfall in NEB (not shown). Therefore, we will not discuss the latter two simulations.

453

### 454 *5.3 Modelled ZASTRF anomalies*

455 To confirm the IFs results and, thus, assess the origin of the atmospheric circulation anomalies that  
456 most contributed to above-normal rainfall in NEB in March 2019, we carried out a set of model experiments  
457 that considered the following combinations among the different TFs (diabatic heating anomalies – Fig. 8):  
458 (i) TFs 2 and 3; (ii) TFs 2–4; (iii) TFs 1–4; and (iv) TFs 1–5. Because the dynamical framework within the  
459 LBM employed is simplified, we only focussed on the qualitative aspect of the model results.

460 The dipole-like TF over the western South Pacific (TF2+TF3 in Fig. 8) generated a teleconnection  
461 pattern that connects the extratropical South Pacific to South Atlantic (TF2+TF3 in Fig. 9). These circulation  
462 anomalies have a barotropic structure over the central-southeastern South Pacific and a baroclinic structure  
463 over the South America–South Atlantic sector. Experiments using TF2 and TF3 separately showed that  
464 TF2 generated circulation anomalies over the South Atlantic through tropical wave dispersion, whilst TF3  
465 triggered extratropical circulation anomalies (not shown). By combining TF4 with TF2 and TF3, results  
466 improve and show a baroclinic circulation over the South Atlantic (TF2+TF3+TF4 in Fig. 9) that more closely  
467 resembles the one observed in the reanalysis data (compare to March panels of Fig. 6 – note that colour  
468 scales are different to allow better visualisation). Such improvement indicates that this baroclinic circulation  
469 is modulated by enhanced rainfall (more condensation heating – TF4 in Fig. 8) in the tropical South Atlantic,  
470 which, in turn, is likely caused by the warmer SST underneath (Fig. 4). The inclusion of TF1 as the fourth  
471 model forcing generates upper-level (200 hPa) positive ZASTRF anomalies to the north of NEB northern  
472 coastline (TF1+TF2+TF3+TF4 in Fig. 9), as seen in the reanalysis data (Fig. 6). When used as the only  
473 model forcing, TF1 (diabatic heating anomalies over the equatorial Pacific – Fig. 8) induces a baroclinic  
474 circulation over the tropical South Atlantic (cyclonic at 200 hPa and anticyclonic at 850 hPa – not shown).  
475 This circulation pattern contrasts the one observed in the reanalysis data (Fig. 6). Similar results were  
476 obtained by Grimm (2019), who employed a barotropic vorticity model forced by divergence sources. By  
477 considering the five TFs together, the lower-level circulation (850 hPa) over the equatorial Atlantic improves  
478 slightly (TF1+TF2+TF3+TF4+TF5 in Fig. 9), resembling the one seen in the reanalysis data a bit more (Fig.

479 6). Therefore, this set of experiments suggests that remote and local forcings jointly modulated the  
480 circulation anomalies that resulted in above-normal rainfall in NEB, as indicated by the IFs results.

481

482

### 483 **6. MJO contributions to the MAM 2019 rainfall in NEB**

484 To further explore mechanisms that may have led to above-normal rainfall in NEB in MAM 2019,  
485 we examined MJO-related conditions in that period. Fig. 10 shows the RMM diagram (Wheeler and Hendon  
486 2004) for March, April, and May 2019. MJO phases 2 and 3 occurred in the first five days of March and the  
487 period 20–27 April. These MJO phases increase the chances of heavier rainfall in NEB (Alvarez et al. 2016;  
488 Grimm 2019) – we note that the effects associated with a given MJO phase may last up to about ten days  
489 after this phase ends (Seo and Son 2012; Seo and Lee 2017), which likely prolonged the influence of the  
490 effects related to MJO phases 2 and 3 on rainfall in NEB in March 2019. In fact, March was the wettest  
491 month of MAM 2019 in the northern portion of NEB, with ~60% of the weather stations analysed presenting  
492 extreme rainfall (Fig. 5). In April 2019, extreme rainfall occurred at ~40% of the stations. MJO-related  
493 convection locates in more northern latitudes from April to September (Adames et al. 2016), accompanying  
494 the ITCZ cloud band displacement. This may have contributed to decreasing the number of stations that  
495 recorded extreme rainfall in April 2019, relative to the previous month. Although MJO phase 2 took place  
496 in the last two days of May 2019, MJO-related convection does not seem to have influenced rainfall in NEB  
497 substantially in that month.

498 As MJO-related convection seems to have played a more decisive role in NEB rainfall amounts in  
499 March 2019, in comparison to the subsequent two months, we now focus on that month and analyse OLR  
500 anomalies filtered at different timescales. Low-frequency signals (>90 days) by themselves do not explain  
501 all unfiltered OLR anomalies (Fig. 11), suggesting a contribution of oscillations at other timescales to the  
502 modulation of atmospheric convection processes. Sub-seasonal signals (30–90 days) for March 2019  
503 indicate reduced convection over NEB, on average, except right over part of the NEB northern coastline.  
504 Positive OLR anomalies (reduced convection) over the western tropical Pacific (~10°S–15°S) at this  
505 timescale seem to reinforce low-frequency anomalies over that area. This reinforcement results in  
506 anomalous upper- and lower-level circulation conditions that favour the formation of an anticyclone and a  
507 cyclone, respectively, over eastern South America and part of the South Atlantic, as found in the model  
508 response to TF2 (not shown). As a consequence, such circulation conditions favour anomalous rainfall  
509 occurrence in NEB, as previously stated. In opposition to monthly-averaged sub-seasonal signals (30–90  
510 days), those averaged over the first ten days of March 2019 indicate that convection was taking place over  
511 the northern portion of NEB. These days were, therefore, the period in which sub-seasonal OLR anomalies  
512 over NEB contributed to strengthening low-frequency signals, which resulted in above-normal rainfall in that  
513 region. Thus, MJO-related sub-seasonal signals very likely contributed to inhibiting deep atmospheric  
514 convection formation over the western tropical Pacific (TF2 region in Fig. 8) during March, as a whole, and  
515 to developing convection over NEB during the first ten days of the month.

516

517

## 518 **7. Conclusions**

519           Understanding the differences between rainfall conditions during El Niño events is essential to  
520 water resources management, agriculture, livestock, and the safety of people and infrastructure. In 2019,  
521 NEB experienced heavy rainfall in autumn (except for the easternmost portion), contrasting the dry  
522 conditions that typically take place during El Niños. To investigate this rainfall anomaly, we analysed  
523 atmospheric and oceanic conditions using several datasets, which allowed us to realise that above-normal  
524 rainfall in NEB in autumn 2019 was likely associated with three main combined factors; these are: (1) the  
525 weak intensity of the 2019 El Niño (as stated by Johnson et al. 2019 and Hu et al. 2020); (2) local and  
526 remote diabatic heating anomalies, especially over the western South Pacific and tropical South Atlantic;  
527 and (3) MJO fluctuations during the first ten days of March 2019.

528           As reported in previous work, the 2019 El Niño was only weak and associated with an anomalous  
529 SST gradient between the western and central equatorial Pacific waters (Johnson et al. 2019). Such a  
530 gradient delayed the El Niño-related ocean-atmosphere coupling development (Johnson et al. 2019),  
531 contributing to different impacts in remote areas from those expected during these events. In certain  
532 regions, such as NEB, atmospheric conditions behaved oppositely those generally observed during El  
533 Niños. Concurrent diabatic heating anomalies over several regions during March 2019 resulted in  
534 anticyclonic and cyclonic circulations in the upper and lower troposphere, respectively, over the tropical  
535 South Atlantic that induced ascending motion over NEB. Deep cooling anomalies (below-normal rainfall)  
536 were observed over the tropical South Pacific, whereas deep heating anomalies (heavier rainfall) occurred  
537 near the eastern/southeastern coast of Australia (over the Tasman Sea). Local effects resulted mainly from  
538 deep heating anomalies over the tropical South Atlantic. Two more thermal forcings contributed to the  
539 circulation that affected rainfall over NEB in March 2019. Deep heating anomalies over the equatorial Pacific  
540 influenced mostly the upper-level (200 hPa) circulation over the seaward area to the north of NEB, whilst  
541 shallow cooling anomalies over the equatorial Atlantic, to the north of NEB northern coast, impacted chiefly  
542 the lower-level (850 hPa) circulation over the tropical South Atlantic. All these anomalous thermal forcings  
543 combined generated deep convection over NEB and caused anomalously heavy rainfall, especially in the  
544 northern portion. MJO phases 2 and 3 coincided with sub-seasonal oscillations that intensified low-  
545 frequency atmospheric convection anomalies over the western Pacific in March 2019 and over NEB during  
546 the first ten days of the month, suggesting, therefore, an influence of MJO-related atmospheric convection  
547 on NEB rainfall in that period.

548           Daily rainfall data may help elucidate how MJO fluctuations contributed to rainfall in NEB in autumn  
549 2019. For instance, ~39% of the March 2019 accumulated rainfall at São Luís station (321.6 mm, out of  
550 818.2 mm) occurred during the first ten days of the month (not shown), when MJO phases were favourable  
551 to increased rainfall in the region. This rainfall amount summed to that of an isolated event on 24 March  
552 2019 (234.4 mm) totalises ~68% of the accumulated rainfall in that month (556.0 mm). Relationships

553 between rainfall in NEB and the ITCZ cloud band during the period analysed here are also worthy of  
554 investigation, given that previous studies have found a significant correlation between them (e.g., Utida et  
555 al. 2019). A more complex numeric model than the one we employed here, which allows for using SST  
556 fields as boundary conditions, may provide more realistic atmospheric responses regarding how equatorial  
557 Atlantic warm SST influences the ITCZ cloud band and, consequently, rainfall in NEB. Nevertheless, our  
558 results complement findings of the previous studies that characterised less common El Niño events (e.g.,  
559 McPhaden 2015; Johnson et al. 2019; Hu et al. 2020), marked by ocean-atmosphere decoupling at initial  
560 stages, such as those that occurred in 1979–1980, 2004–2005, 2014–2015, and 2018–2019 (Hu et al.  
561 2020). Our results also support the conclusion by Hu et al. (2020) that states that El Niño-related rainfall  
562 anomalies cannot be predicted accurately based solely on SST anomalies in the tropical Pacific.  
563 Atmosphere-ocean coupling is crucial to trigger remote rainfall anomalies. Even when the coupling takes  
564 place, like during the period analysed here, rainfall anomalies may not follow the expected pattern for El  
565 Niño. This rainfall behaviour has been reported here, reinforcing how much ENSO-related anomalies matter  
566 to rainfall occurrence and intensity in NEB. Besides the ENSO's phase (El Niño or La Niña) and flavour  
567 (canonical or Modoki), the intensity of its associated anomalies is of paramount importance to determine  
568 whether drought or above-normal rainfall should be expected in NEB.

569

570

## 571 **Acknowledgements**

572 The authors are thankful to INMET ([www.inmet.gov.br](http://www.inmet.gov.br)), ECMWF  
573 (<https://apps.ecmwf.int/datasets/data/interim-full-moda/levtype=sfc/>), and NOAA  
574 (<https://psl.noaa.gov/data/gridded/data.noaa.ersst.v5.html>,  
575 <https://psl.noaa.gov/data/gridded/data.gpcp.html>, and  
576 [https://psl.noaa.gov/data/gridded/data.interp\\_OLR.html](https://psl.noaa.gov/data/gridded/data.interp_OLR.html)) for providing the data employed in this research.  
577 We also thank Dr Steven Woolnough, for providing the code to plot the RMM diagram, Dr José Aravéquia,  
578 for providing the code to compute influence functions, Dr Michiya Hayashi and Dr Masahiro Watanabe, for  
579 providing the LBM code (<https://ccsr.ori.u-tokyo.ac.jp/~lbm/sub/lbm.html>), and the reviewers, for the  
580 constructive comments.

581

582

## 583 **References**

584 Adames ÁF, Wallace JM, Monteiro JM (2016) Seasonality of the structure and propagation characteristics  
585 of the MJO. *J. Atmos. Sci.* 73:3511–3526. <https://doi.org/10.1175/JAS-D-15-0232.1>

586

587 Adler RF, Sapiano MRP, Huffman GJ, Wang J-J, Gu G, Bolvin D, Chiu L, Schneider U, Becker A, Nelkin  
588 E, Xie P, Ferraro R, Shin D-B (2018) The Global Precipitation Climatology Project (GPCP) monthly analysis

589 (new version 2.3) and a review of 2017 global precipitation. *Atmosphere* 9(4)138.  
590 <https://doi.org/10.3390/atmos9040138>  
591

592 Allen MP (1997) The t test for the simple regression coefficient. In: *Understanding regression analysis*.  
593 Springer, Boston, MA. 66–70. [https://doi.org/10.1007/978-0-585-25657-3\\_14](https://doi.org/10.1007/978-0-585-25657-3_14)  
594

595 Alvarez MS, Vera CS, Kiladis GN, Liebmann B (2016) Influence of the Madden Julian Oscillation on  
596 precipitation and surface air temperature in South America. *Clim. Dyn.* 46:245–262.  
597 <https://doi.org/10.1007/s00382-015-2581-6>  
598

599 Ambrizzi T, Hoskins BJ (1997) Stationary Rossby-wave propagation in a baroclinic atmosphere. *Q. J. R.*  
600 *Meteorol. Soc.* 123(540):919–928. <https://doi.org/10.1002/qj.49712354007>  
601

602 Ashok K, Behera SK, Rao SA, Weng H, Yamagata T (2007) El Niño Modoki and its possible teleconnection.  
603 *J. Geophys. Res.: Oceans* 112(C11007). <https://doi.org/10.1029/2006JC003798>  
604

605 Bjerknes J (1961) “El Niño” study based on analysis of ocean surface temperatures 1935–57. *Inter-Am.*  
606 *Trop. Tuna Comm. Bull.* 5(3):217–303.  
607

608 Bjerknes J (1966) A possible response of the atmospheric Hadley circulation to equatorial anomalies of  
609 ocean temperature. *Tellus* 18(4):820–829. <https://doi.org/10.1111/j.2153-3490.1966.tb00303.x>  
610

611 Branstator G (1985) Analysis of general circulation model sea-surface temperature anomaly simulations  
612 using a linear model. Part I: forced solutions. *Journal of the Atmospheric Sciences* 42(21): 2225–2241.  
613 [https://doi.org/10.1175/1520-0469\(1985\)042<2225:AOGCMS>2.0.CO;2](https://doi.org/10.1175/1520-0469(1985)042<2225:AOGCMS>2.0.CO;2)  
614

615 Cai W, Cowan T (2008) Dynamics of late autumn rainfall reduction over southeastern Australia. *Geophys.*  
616 *Res. Lett.* 35(9):L09708. <https://doi.org/10.1029/2008GL033727>  
617

618 Cai W, McPhaden MJ, Grimm AM, Rodrigues RR, Taschetto AS, Garreaud RD, Dewitte B, Poveda G, Ham  
619 Y-G, Santoso A, Ng B, Anderson W, Wang G, Geng T, Jo H-S, Marengo JA, Alves LM, Osman M, Li S, Wu  
620 L, Karamperidou C, Takahashi K, Vera C (2020) Climate impacts of the El Niño–Southern Oscillation on  
621 South America. *Nat. Rev. Earth Environ.* 1:215–231. <https://doi.org/10.1038/s43017-020-0040-3>  
622

623 Cai W, van Rensch P, Cowan T (2011) Teleconnection pathways of ENSO and the IOD and the  
624 mechanisms for impacts on Australian rainfall. *J. Clim.* 24:3910–3923.  
625 <https://doi.org/10.1175/2011JCLI4129.1>

626  
627 Cane MA (2005) The evolution of El Niño, past and future. *Earth Planet. Sci. Lett.* 230(3–4):227–240.  
628 <https://doi.org/10.1016/j.epsl.2004.12.003>  
629  
630 Chase TN, Pielke Sr RA, Avissa R (2006) Teleconnections in the Earth System. In: Anderson MG (ed)  
631 *Encyclopedia of Hydrological Sciences*. Wiley, Hoboken. <https://doi.org/10.1002/0470848944.hsa190>  
632  
633 Davey MK, Brookshaw A, Ineson S (2014) The probability of the impact of ENSO on precipitation and near-  
634 surface temperature. *Clim. Risk Manag.* 1:5–24. <https://doi.org/10.1016/j.crm.2013.12.002>  
635  
636 Dee DP et al (2011) The ERA-Interim reanalysis: configuration and performance of the data assimilation  
637 system. *Q. J. R. Meteorol. Soc.* 137:553–597. <https://doi.org/10.1002/qj.828>  
638  
639 Duchon CE (1979) Lanczos filtering in one and two dimensions. *J. Appl. Meteorol. Climatol.* 18(8):1016–  
640 1022. [https://doi.org/10.1175/1520-0450\(1979\)018<1016:LFIOAT>2.0.CO;2](https://doi.org/10.1175/1520-0450(1979)018<1016:LFIOAT>2.0.CO;2)  
641  
642 Giovannettone J, Paredes-Trejo F, Barbosa H, dos Santos CA, Kumar TVL (2020) Characterization of links  
643 between hydro-climate indices and long-term precipitation in Brazil using correlation analysis. *Int. J.*  
644 *Climatol.* 40(13):5527–5541. <https://doi.org/10.1002/joc.6533>  
645  
646 Grimm AM (2003) The El Niño impact on the summer monsoon in Brazil: regional processes versus remote  
647 influences. *J. Clim.* 16(2):263–280. [https://doi.org/10.1175/1520-0442\(2003\)016<0263:TENIOT>2.0.CO;2](https://doi.org/10.1175/1520-0442(2003)016<0263:TENIOT>2.0.CO;2)  
648  
649 Grimm AM (2011) Interannual climate variability in South America: impacts on seasonal precipitation,  
650 extreme events, and possible effects of climate change. *Stoch Environ Res Risk Assess* 25:537–554.  
651 <https://doi.org/10.1007/s00477-010-0420-1>  
652  
653 Grimm AM (2018) South American monsoon and its extremes. In: Vuruputur V, Sukhatme J, Murtugudde  
654 R, Roca R (eds) *Tropical extremes: natural variability and trends*. Elsevier, Amsterdam, Chapter 3, pp 51–  
655 93. <https://doi.org/10.1016/B978-0-12-809248-4.00003-0>  
656  
657 Grimm AM (2019) Madden–Julian Oscillation impacts on South American summer monsoon season:  
658 precipitation anomalies, extreme events, teleconnections, and role in the MJO cycle. *Clim. Dyn.*, 53(1):907–  
659 932. <https://doi.org/10.1007/s00382-019-04622-6>  
660  
661 Grimm AM, Almeida AS, Beneti CAA, Leite EA (2020) The combined effect of climate oscillations in  
662 producing extremes: the 2020 drought in southern Brazil. *Brazilian Journal of Water Resources* 25:e48.  
663 <https://doi.org/10.1590/2318-0331.252020200116>

664

665 Grimm AM, Ambrizzi T (2009) Teleconnections into South America from the tropics and extratropics on  
666 interannual and intraseasonal timescales. In: Vimeux F, Sylvestre F, Khodri M (eds) Past climate variability  
667 in South America and surrounding regions. Developments in paleoenvironmental research. Springer,  
668 Dordrecht, pp 159–191. [https://doi.org/10.1007/978-90-481-2672-9\\_7](https://doi.org/10.1007/978-90-481-2672-9_7)

669

670 Grimm AM, Reason CJC (2011) Does the South American monsoon influence African rainfall? *J. Clim.*  
671 24(4):1226–1238. <https://doi.org/10.1175/2010JCLI3722.1>

672

673 Grimm AM, Reason CJC (2015) Intraseasonal teleconnections between south america and south africa. *J.*  
674 *Clim.* 28(23):9489–9497. <https://doi.org/10.1175/JCLI-D-15-0116.1>

675

676 Grimm AM, Silva Dias PL (1995) Analysis of tropical–extratropical interactions with influence functions of a  
677 barotropic model. *J. Atmos. Sci.* 52(20):3538–3555. [https://doi.org/10.1175/1520-  
678 0469\(1995\)052<3538:AOTIWI>2.0.CO;2](https://doi.org/10.1175/1520-0469(1995)052<3538:AOTIWI>2.0.CO;2)

679

680 Houze RA (2014) Cumulonimbus and severe storms. *Cloud Dynamics* 104:187–236.  
681 <https://doi.org/10.1016/B978-0-12-374266-7.00008-1>

682

683 Hu ZZ, McPhaden MJ, Kumar A, Yu JY, Johnson NC (2020) Uncoupled El Niño warming. *Geophys. Res.*  
684 *Lett.* 47(7):.e2020GL087621. <https://doi.org/10.1029/2020GL087621>

685

686 Huang B, Thorne PW, Banzon VF, Boyer T, Chepurin G, Lawrimore JH, Menne MJ, Smith TM, Vose RS,  
687 Zhang H-M (2017) Extended reconstructed sea surface temperature, version 5 (ERSSTv5): upgrades,  
688 validations, and intercomparisons. *J. Clim.* 30(20):8179–8205. <https://doi.org/10.1175/JCLI-D-16-0836.1>

689

690 Jin F, Hoskins BJ (1995) The direct response to tropical heating in a baroclinic atmosphere. *J. Atmos. Sci.*  
691 52(3):307–319. [https://doi.org/10.1175/1520-0469\(1995\)052<0307:TDRTH>2.0.CO;2](https://doi.org/10.1175/1520-0469(1995)052<0307:TDRTH>2.0.CO;2)

692

693 Johnson NC, L'Heureux ML, Chang C-H, Hu Z-Z (2019) On the delayed coupling between ocean and  
694 atmosphere in recent weak El Niño episodes. *Geophys. Res. Lett.* 46:11416–11425.  
695 <https://doi.org/10.1029/2019GL084021>

696

697 Kasahara A, Silva Dias PL (1986) Response of planetary waves to stationary tropical heating in a global  
698 atmosphere with meridional and vertical shear. *J. Atmos. Sci.* 43(18):1893–1912.  
699 [https://doi.org/10.1175/1520-0469\(1986\)043<1893:ROPWTS>2.0.CO;2](https://doi.org/10.1175/1520-0469(1986)043<1893:ROPWTS>2.0.CO;2)

700

701 Kayano MT, Capistrano VB (2014) How the Atlantic multidecadal oscillation (AMO) modifies the ENSO  
702 influence on the South American rainfall. *Int. J. Climatol.* 34(1):162–178. <https://doi.org/10.1002/joc.3674>  
703

704 Levine AF, McPhaden MJ, Frierson DM (2017) The impact of the AMO on multidecadal ENSO variability.  
705 *Geophys. Res. Lett.* 44(8):3877–3886. <https://doi.org/10.1002/2017GL072524>  
706

707 L'Heureux ML, Takahashi K, Watkins AB, Barnston AG, Becker EJ, Di Liberto TE, Gamble F, Gottschalck  
708 J, Halpert MS, Huang B, Mosquera-Vásquez K, Wittenberg AT (2017) Observing and predicting the 2015/16  
709 El Niño. *Bull. Am. Meteorol. Soc.* 98(7):1363–1382. <https://doi.org/10.1175/BAMS-D-16-0009.1>  
710

711 L'Heureux ML, Thompson DWJ (2006) Observed relationships between the El Niño–Southern Oscillation  
712 and the extratropical zonal-mean circulation. *J. Clim.* 19:276–287. <https://doi.org/10.1175/JCLI3617.1>  
713

714 Liebmann B, Smith CA (1996) Description of a complete (interpolated) outgoing longwave radiation dataset.  
715 *Bull. Am. Meteorol. Soc.* 77(6):1275–1277  
716

717 Lin J, Qian TA (2019) A new picture of the global impacts of El Niño–Southern Oscillation. *Sci. Rep.* 9  
718 17543. <https://doi.org/10.1038/s41598-019-54090-5>  
719

720 Liu AZ, Ting M, Wang H (1998) Maintenance of circulation anomalies during the 1988 drought and 1993  
721 floods over the United States. *J. Atmos. Sci.* 55(17):2810–2832. [https://doi.org/10.1175/1520-  
722 0469\(1998\)055<2810:MOCADT>2.0.CO;2](https://doi.org/10.1175/1520-0469(1998)055<2810:MOCADT>2.0.CO;2)  
723

724 Livezey RE, Chen WY (1983) Statistical field significance and its determination by Monte Carlo techniques.  
725 *Mon. Wea. Rev.* 111(1):46–59. [https://doi.org/10.1175/1520-0493\(1983\)111<0046:SFSRID>2.0.CO;2](https://doi.org/10.1175/1520-0493(1983)111<0046:SFSRID>2.0.CO;2)  
726

727 Lo F, Hendon HH (2000) Empirical extended-range prediction of the Madden–Julian Oscillation. *Mon. Wea.*  
728 *Rev.* 128(7):2528–2543. [https://doi.org/10.1175/1520-0493\(2000\)128<2528:EERPOT>2.0.CO;2](https://doi.org/10.1175/1520-0493(2000)128<2528:EERPOT>2.0.CO;2)  
729

730 Madden RA, Julian PR (1971) Detection of a 40–50 day oscillation in the zonal wind in the tropical Pacific.  
731 *J. Atmos. Sci.* 28:702–708. [https://doi.org/10.1175/1520-0469\(1971\)028<0702:DOADOI>2.0.CO;2](https://doi.org/10.1175/1520-0469(1971)028<0702:DOADOI>2.0.CO;2)  
732

733 Madden RA, Julian PR (1972) Description of global-scale circulation cells in the tropics with a 40–50 day  
734 period. *J. Atmos. Sci.* 29:1109–1123. [https://doi.org/10.1175/1520-  
735 0469\(1972\)029<1109:DOGSCC>2.0.CO;2](https://doi.org/10.1175/1520-0469(1972)029<1109:DOGSCC>2.0.CO;2)  
736

737 Madden RA, Julian PR (1994) Observations of the 40–50-day tropical oscillation—a review. *Mon. Wea.*  
738 *Rev.* 122:814–837. [https://doi.org/10.1175/1520-0493\(1994\)122<0814:OOTDTO>2.0.CO;2](https://doi.org/10.1175/1520-0493(1994)122<0814:OOTDTO>2.0.CO;2)  
739

740 Majda AJ, Biello JA (2003) The nonlinear interaction of barotropic and equatorial baroclinic Rossby waves.  
741 *J. Atmos. Sci.* 60(15):1809–1821. [https://doi.org/10.1175/1520-0469\(2003\)060<1809:TNIOPA>2.0.CO;2](https://doi.org/10.1175/1520-0469(2003)060<1809:TNIOPA>2.0.CO;2)  
742

743 Mantua NJ, Hare SR (2002) The Pacific Decadal Oscillation. *J. Oceanogr.* 58:35–44.  
744 <https://doi.org/10.1023/A:1015820616384>  
745

746 McPhaden MJ (2015) Playing hide and seek with El Niño. *Nat. Clim. Change* 5:791–795.  
747 <https://doi.org/10.1038/nclimate2775>  
748

749 McPhaden MJ, Zebiak SE, Glantz MH (2006) ENSO as an integrating concept in Earth science. *Science*  
750 314(5806):1740–1745. <https://doi.org/10.1126/science.1132588>  
751

752 Mo KC, Nogues-Paegle J (2005) Pan-America. Intraseasonal variability in the atmosphere-ocean climate  
753 system. Springer Praxis Books (Environmental Sciences). Springer, Berlin, Heidelberg, pp 95–124.  
754 [https://doi.org/10.1007/3-540-27250-X\\_4](https://doi.org/10.1007/3-540-27250-X_4)  
755

756 Neelin JD, Battisti DS, Hirst AC, Jin F-F, Wakata Y, Yamagata T, Zebiak SE (1998) ENSO theory. *J.*  
757 *Geophys. Res. Oceans* 103(C7):14261–14290. <https://doi.org/10.1029/97JC03424>  
758

759 Nicholls N (1985) Towards the prediction of major Australian droughts. *Aust. Met. Mag.* 33:161–166  
760

761 Nicholls N (1991) The El Niño / Southern Oscillation and Australian vegetation. *Vegetatio* 91(1–2):23–36.  
762 <https://doi.org/10.1007/BF00036045>  
763

764 Nobre GG, Muis S, Veldkamp TI, Ward PJ (2019) Achieving the reduction of disaster risk by better  
765 predicting impacts of El Niño and La Niña. *Progress in Disaster Science* 2:100022.  
766 <https://doi.org/10.1016/j.pdisas.2019.100022>  
767

768 Rodrigues RR, Haarsma RJ, Campos EJD, Ambrizzi T (2011) The impacts of inter–El Niño variability on  
769 the tropical Atlantic and northeast Brazil climate. *J. Clim.* 24:3402–3422.  
770 <https://doi.org/10.1175/2011JCLI3983.1>  
771

772 Rodrigues RR, McPhaden MJ (2014) Why did the 2011–2012 La Niña cause a severe drought in the  
773 Brazilian Northeast? *Geophys. Res. Lett.* 41:1012–1018. <https://doi.org/10.1002/2013GL058703>

774  
775 Schumacher C, Houze Jr, RA, Kraucunas I (2004) The tropical dynamical response to latent heating  
776 estimates derived from the TRMM precipitation radar. *Journal of the Atmospheric Sciences* 61(12):1341–  
777 1358. [https://doi.org/10.1175/1520-0469\(2004\)061<1341:TTDRTL>2.0.CO;2](https://doi.org/10.1175/1520-0469(2004)061<1341:TTDRTL>2.0.CO;2)  
778  
779 Schumacher C, Zhang MH, Ciesielski PE (2007) Heating structures of the TRMM field campaigns. *J. Atmos.*  
780 *Sci.* 64(7):2593–2610. <https://doi.org/10.1175/JAS3938.1>  
781  
782 Seo K-H, Lee HJ (2017) Mechanisms for a PNA-like teleconnection pattern in response to the MJO. *J.*  
783 *Atmos. Sci.* 74(6):1767–1781. <https://doi.org/10.1175/JAS-D-16-0343.1>  
784  
785 Seo K-H, Son S-W (2012) The global atmospheric circulation response to tropical diabatic heating  
786 associated with the Madden–Julian Oscillation during northern winter. *J. Atmos. Sci.* 69(1):79–96.  
787 <https://doi.org/10.1175/2011JAS3686.1>  
788  
789 Shimizu MH, Ambrizzi T (2016) MJO influence on ENSO effects in precipitation and temperature over South  
790 America. *Theor. Appl. Climatol.* 124:291–301. <https://doi.org/10.1007/s00704-015-1421-2>  
791  
792 Shimizu MH, Ambrizzi T, Liebmann B (2017) Extreme precipitation events and their relationship with ENSO  
793 and MJO phases over northern South America. *Int. J. Climatol.* 37(6):2977–2989.  
794 <https://doi.org/10.1002/joc.4893>  
795  
796 Shimizu MH, Cavalcanti IFA (2011) Variability patterns of Rossby wave source. *Clim. Dyn.* 37:441–454.  
797 <https://doi.org/10.1007/s00382-010-0841-z>  
798  
799 Stan C, Straus DM, Frederiksen JS, Lin H, Maloney ED, Schumacher C (2017) Review of tropical-  
800 extratropical teleconnections on intraseasonal time scales. *Rev. Geophys.* 55(4):902–937.  
801 <https://doi.org/10.1002/2016RG000538>  
802  
803 Taschetto AS, England MH (2009) El Niño Modoki impacts on Australian rainfall. *J. Clim.* 22:3167–3174.  
804 <https://doi.org/10.1175/2008JCLI2589.1>  
805  
806  
807 Tedeschi RG, Grimm AM, Cavalcanti IFA (2015) Influence of Central and East ENSO on extreme events  
808 of precipitation in South America during austral spring and summer. *Int. J. Climatol.* 35(8):2045–2064.  
809 <https://doi.org/10.1002/joc.4106>  
810

811 Tedeschi RG, Grimm AM, Cavalcanti IFA (2016) Influence of Central and East ENSO on precipitation and  
812 its extreme events in South America during austral autumn and winter. *Int. J. Climatol.* 36(15):4797–4814.  
813 <https://doi.org/10.1002/joc.4670>  
814

815 Teng H, Branstator G (2019) Amplification of waveguide teleconnections in the boreal summer. *Curr Clim*  
816 *Change Rep* 5(4):421–432. <https://doi.org/10.1007/s40641-019-00150-x>  
817

818 Trenberth KE (1997) The definition of el nino. *Bulletin of the American Meteorological Society* 78(12):2771–  
819 2778. [https://doi.org/10.1175/1520-0477\(1997\)078<2771:TDOENO>2.0.CO;2](https://doi.org/10.1175/1520-0477(1997)078<2771:TDOENO>2.0.CO;2)  
820

821 Trenberth KE, Caron JM (2000) The Southern Oscillation revisited: sea level pressures, surface  
822 temperatures, and precipitation. *J. Clim.* 13(24):4358–4365. [https://doi.org/10.1175/1520-0442\(2000\)013<4358:TSORSL>2.0.CO;2](https://doi.org/10.1175/1520-0442(2000)013<4358:TSORSL>2.0.CO;2)  
823  
824

825 Trenberth KE, Hurrell JW (1994) Decadal atmosphere-ocean variations in the Pacific. *Clim. Dyn.* 9(6):303–  
826 319. <https://doi.org/10.1007/BF00204745>  
827

828 Trenberth KE, Solomon A (1993) Implications of global atmospheric spatial spectra for processing and  
829 displaying data. *J. Clim.* 6(3):531–545. [https://doi.org/10.1175/1520-0442\(1993\)006<0531:IOGASS>2.0.CO;2](https://doi.org/10.1175/1520-0442(1993)006<0531:IOGASS>2.0.CO;2)  
830  
831

832 Trenberth KE, Stepaniak DP (2001) Indices of El Niño evolution. *J. Clim.* 14(8):1697–1701.  
833 [https://doi.org/10.1175/1520-0442\(2001\)014<1697:LIOENO>2.0.CO;2](https://doi.org/10.1175/1520-0442(2001)014<1697:LIOENO>2.0.CO;2)  
834

835 Tseng K-C, Maloney E, Barnes EA (2019) The consistency of MJO teleconnection patterns: an explanation  
836 using linear Rossby wave theory. *J. Clim.* 32:531–548. <https://doi.org/10.1175/JCLI-D-18-0211.1>  
837

838 Tseng K-C, Maloney E, Barnes EA (2020) The consistency of MJO teleconnection patterns on interannual  
839 time scales. *J. Clim.* 33(9):3471–3486. <https://doi.org/10.1175/JCLI-D-19-0510.1>  
840

841 Utida G, Cruz FW, Etourneau J, Bouloubassi I, Schefuß E, Vuille M, Novello VF, Prado LF, Sifeddine A,  
842 Klein V, Zular A, Viana JCC, Turcq B (2019) Tropical South Atlantic influence on Northeastern Brazil  
843 precipitation and ITCZ displacement during the past 2300 years. *Scientific reports* 9(1):1–8.  
844 <https://doi.org/10.1038/s41598-018-38003-6>  
845

846 Walker GT, Bliss EW (1932) World weather V. *Mem. R. Meteorol. Soc.* 4(36):53–84  
847

848 Walker GT, Bliss EW (1937) World weather VI. Mem. R. Meteorol. Soc. 4(39):119–139  
849  
850 Wallace JM, Hobbs PV, McMurdie L, Houze RA (2006) Weather Systems. In: Atmospheric Science – An  
851 Introductory Survey, 2nd Edition pp 313–373. <https://doi.org/10.1016/B978-0-12-732951-2.50013-2>  
852  
853 Watanabe M, Kimoto M. (2000) Atmosphere–ocean thermal coupling in the North Atlantic: A positive  
854 feedback. Q. J. R. Meteorol. Soc. 126(570):3343–3369. <https://doi.org/10.1002/qj.49712657017>.  
855  
856 Wheeler MC, Hendon HH (2004) An all-season real-time multivariate MJO index: development of an index  
857 for monitoring and prediction. Mon. Wea. Rev. 132:1917–1932. [https://doi.org/10.1175/1520-  
858 0493\(2004\)132<1917:AARMMI>2.0.CO;2](https://doi.org/10.1175/1520-0493(2004)132<1917:AARMMI>2.0.CO;2)  
859  
860 Wyrski K (1975) El Niño—the dynamic response of the equatorial Pacific Ocean to atmospheric forcing. J.  
861 Phys. Oceanogr. 5:572–584. [https://doi.org/10.1175/1520-0485\(1975\)005<0572:ENTDRO>2.0.CO;2](https://doi.org/10.1175/1520-0485(1975)005<0572:ENTDRO>2.0.CO;2)  
862  
863 Yanai M, Esbensen S, Chu JH (1973) Determination of bulk properties of tropical cloud clusters from large-  
864 scale heat and moisture budgets. J. Atmos. Sci. 30(4):611–627. [https://doi.org/10.1175/1520-  
865 0469\(1973\)030<0611:DOBPO>2.0.CO;2](https://doi.org/10.1175/1520-0469(1973)030<0611:DOBPO>2.0.CO;2)  
866  
867 Zhang C, Hagos SM (2009) Bi-modal structure and variability of large-scale diabatic heating in the tropics.  
868 J. Atmos. Sci. 66(12):3621–3640. <https://doi.org/10.1175/2009JAS3089.1>  
869  
870 Zhou G (2019) Atmospheric Response to Sea Surface Temperature Anomalies in the Mid-latitude Oceans:  
871 A Brief Review. Atmosphere–Ocean 57(5):319–328. <https://doi.org/10.1080/07055900.2019.1702499>  
872  
873

#### 874 **Figure captions**

875 **Fig. 1** Locations of the weather stations in northeastern Brazil from where data were sourced. MA, PI, CE,  
876 and RN stand for Maranhão, Piauí, Ceará, and Rio Grande do Norte, respectively  
877

878 **Fig. 2** Linear regressions of austral autumn sea surface temperature (SST), rainfall, and 200-hPa and 850-  
879 hPa zonally asymmetric streamfunction (ZASTRF) anomalies onto Niño 3.4 index. Hatched areas indicate  
880 statistically significant values at the 90% confidence level according to a two-tailed Student's *t*-test (Allen  
881 1997)  
882

883 **Fig. 3** Linear regressions of austral autumn sea surface temperature (SST), rainfall, and 200-hPa and 850-  
884 hPa zonally asymmetric streamfunction (ZASTRF) anomalies onto El Niño Modoki Index (EMI). Hatched

885 areas indicate statistically significant values at the 90% confidence level according to a two-tailed Student's  
886 *t*-test (Allen 1997)

887

888 **Fig. 4** Sea surface temperature (left panels) and rainfall (right panels) anomalies for March, April, May, and  
889 autumn 2019

890

891 **Fig. 5** Normalised accumulated rainfall anomalies for March, April, May, and autumn over the period 1979–  
892 2019. Anomalies were calculated from weather station data collected in northeastern Brazil. Dashed grey  
893 lines represent  $\pm 1$  standard deviation, and straight grey lines null standard deviation. Vertical dotted lines  
894 mark years of extreme El Niños (1983, 1998, and 2016)

895

896 **Fig. 6** 200-hPa (left panels) and 850-hPa (right panels) zonally asymmetric streamfunction (ZASTRF)  
897 anomalies for March, April, May, and autumn 2019. Black dots represent the target points 1–5 (from left to  
898 right), where circulation anomalies were assessed using the influence functions and LBM (please refer to  
899 Fig. 7 for additional details)

900

901 **Fig. 7** Influence functions results: 200-hPa (left panels) and 850-hPa (right panels) zonally asymmetric  
902 streamfunction (ZASTRF) anomalies for five target points (TP1–TP5 – black dots), considering the March  
903 climatological basic state. IFs were applied to modelled ZASTRF anomalies, between 35°S and 35°N  
904 (straight horizontal lines), on the 15th day of simulation. Magenta [green] contours ( $1 \times 10^6$  m<sup>2</sup>/s) indicate  
905 positive [negative] ZASTRF anomalies around the TP for positive diabatic heating anomalies. Dashed lines  
906 indicate the zero contour

907

908 **Fig. 8** Vertical and horizontal distributions of the diabatic heating anomalies incorporated into the model's  
909 temperature tendency equation. TF stands for thermal forcing

910

911 **Fig. 9** Modelled 200-hPa (left panels) and 850-hPa (right panels) zonally asymmetric streamfunction  
912 (ZASTRF) results on the 15th day of simulation considering combinations among the thermal forcings (TFs)  
913 1, 2, 3, 4, and 5

914

915 **Fig. 10** RMM diagram for March (blue), April (green), and May (red) 2019. Stars and squares represent the  
916 first and last days of the months, respectively. Full circles indicate the other days of the month, in ascending  
917 order, connected by straight lines. The central circle indicates an inactive MJO. Each region comprises the  
918 two MJO phases that are expected to enhance atmospheric convection over that region

919

920 **Fig. 11** Mean outgoing longwave radiation (OLR) for March 2019: (upper panel) unfiltered; (upper-middle  
921 panel) low-frequency filtered (>90 days); (lower-middle panel) sub-seasonally filtered (30–90 days); and  
922 (lower panel) the first ten days of March 2019. Averages were calculated using daily OLR anomalies

# Figures

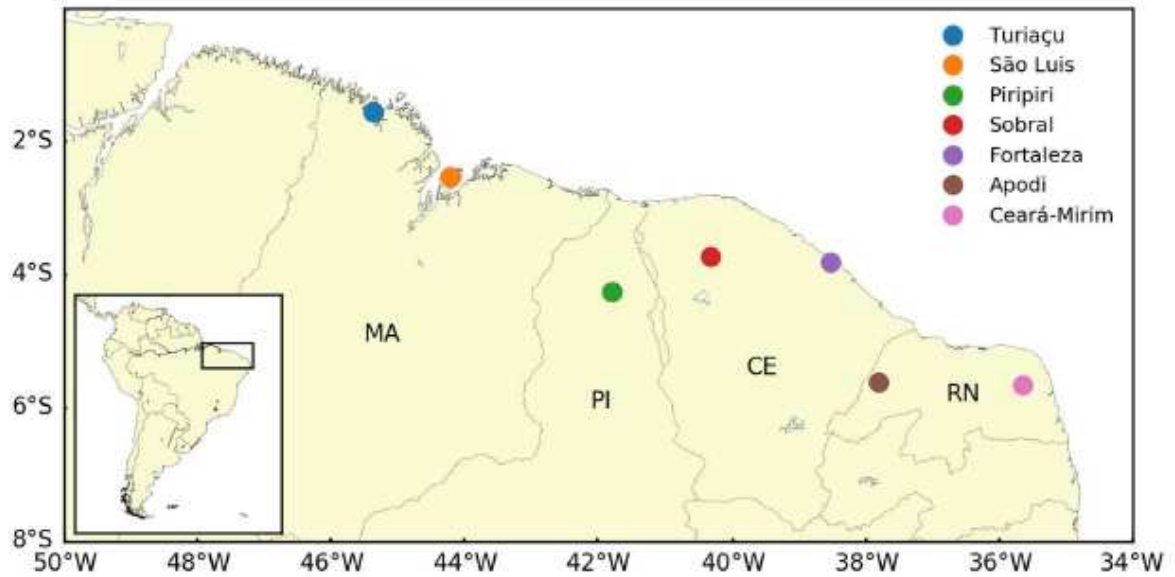


Figure 1

Locations of the weather stations in northeastern Brazil from where data were sourced. MA, PI, CE, and RN stand for Maranhão, Piauí, Ceará, and Rio Grande do Norte, respectively

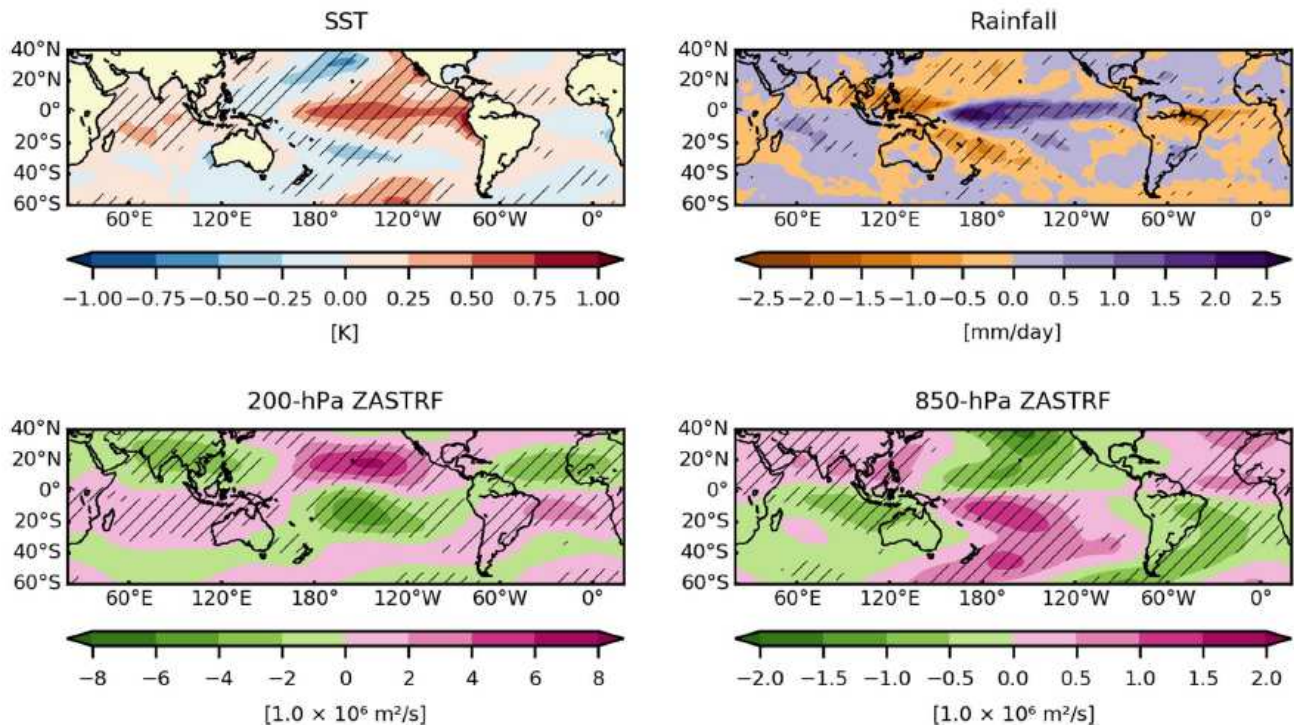
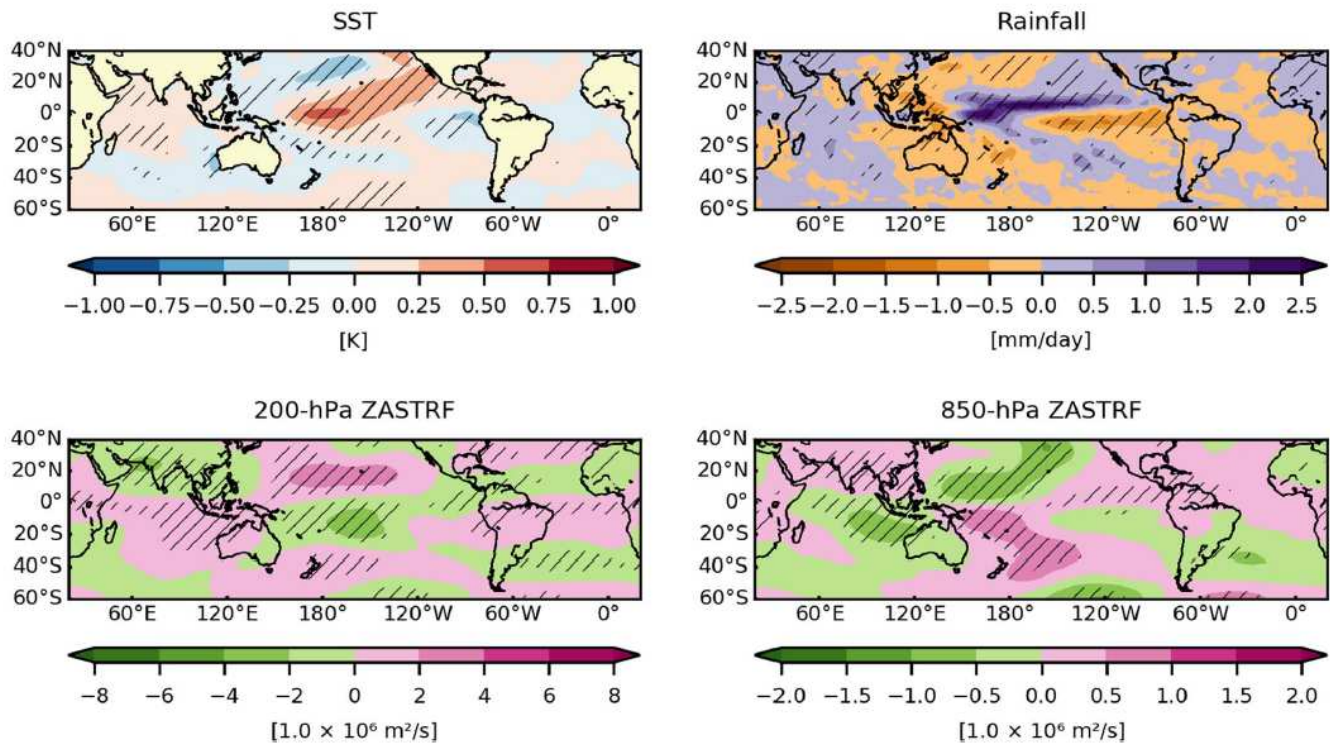


Figure 2

Linear regressions of austral autumn sea surface temperature (SST), rainfall, and 200-hPa and 850-hPa zonally asymmetric streamfunction (ZASTRF) anomalies onto Niño 3.4 index. Hatched areas indicate statistically significant values at the 90% confidence level according to a two-tailed Student's t-test (Allen 1997)



**Figure 3**

Linear regressions of austral autumn sea surface temperature (SST), rainfall, and 200-hPa and 850-hPa zonally asymmetric streamfunction (ZASTRF) anomalies onto El Niño Modoki Index (EMI). Hatched areas indicate statistically significant values at the 90% confidence level according to a two-tailed Student's t-test (Allen 1997)

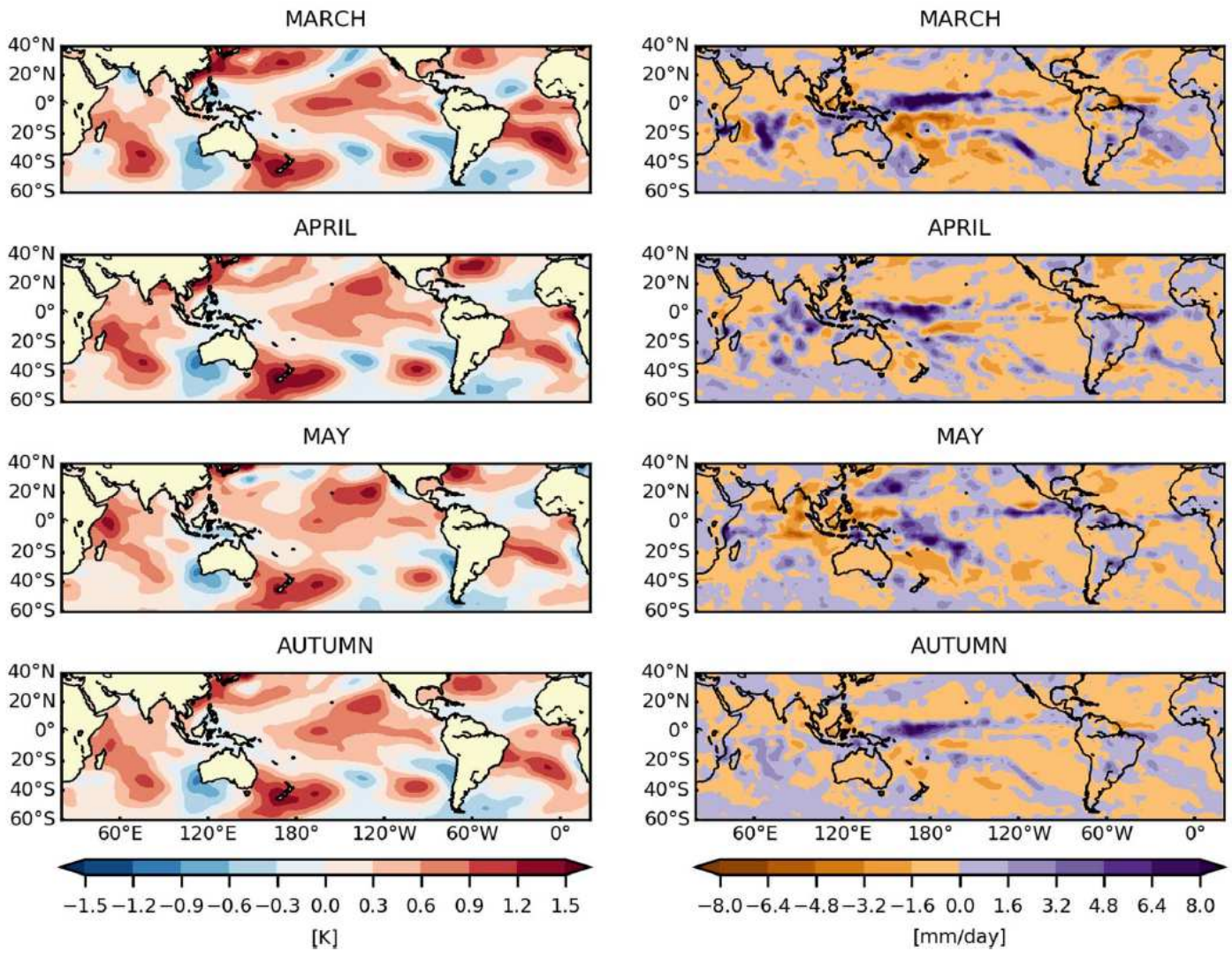


**Figure 4**

Sea surface temperature (left panels) and rainfall (right panels) anomalies for March, April, May, and autumn 2019

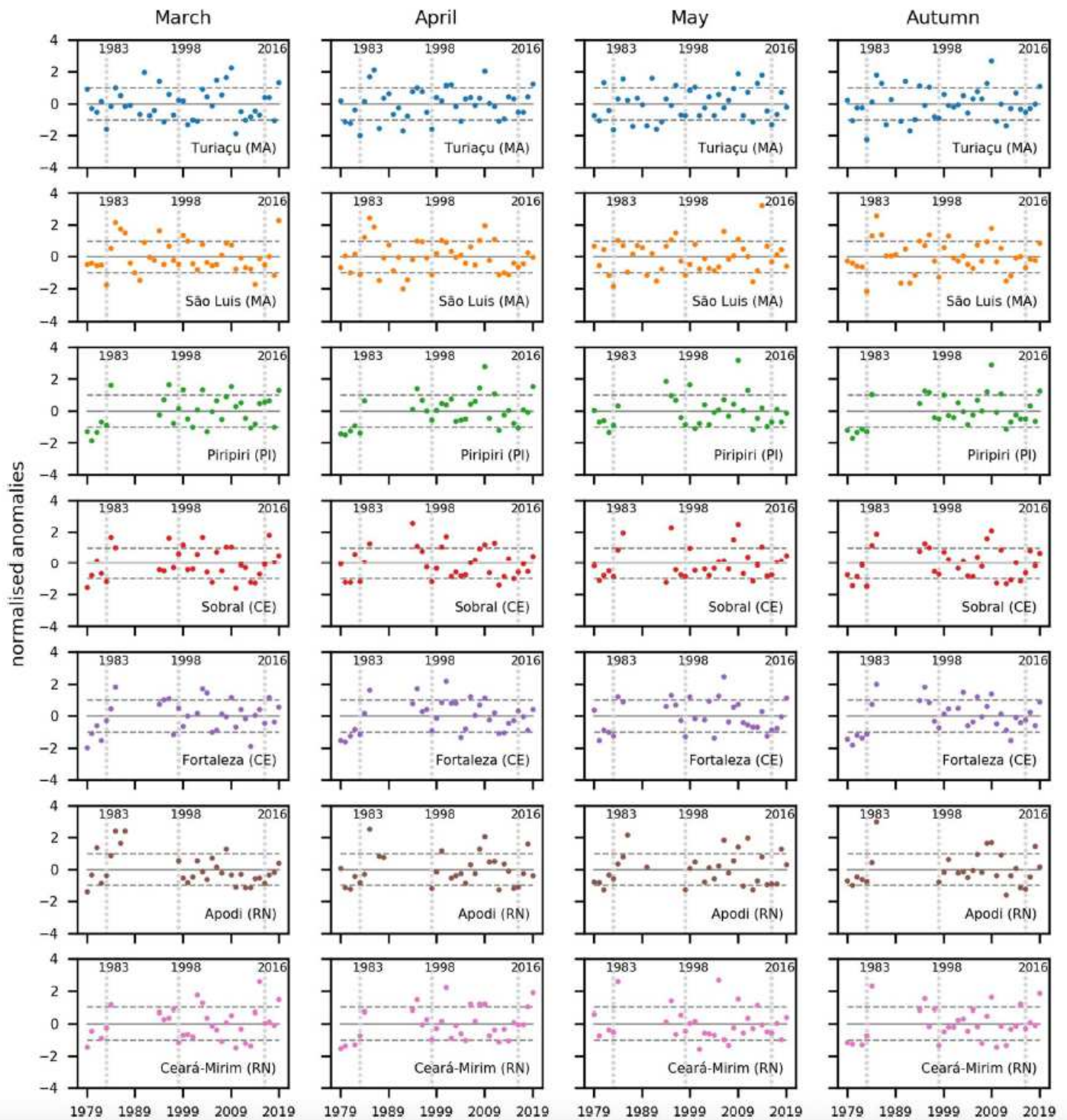


**Figure 5**

Normalised accumulated rainfall anomalies for March, April, May, and autumn over the period 1979–2019. Anomalies were calculated from weather station data collected in northeastern Brazil. Dashed grey lines represent  $\pm 1$  standard deviation, and straight grey lines null standard deviation. Vertical dotted lines mark years of extreme El Niños (1983, 1998, and 2016)

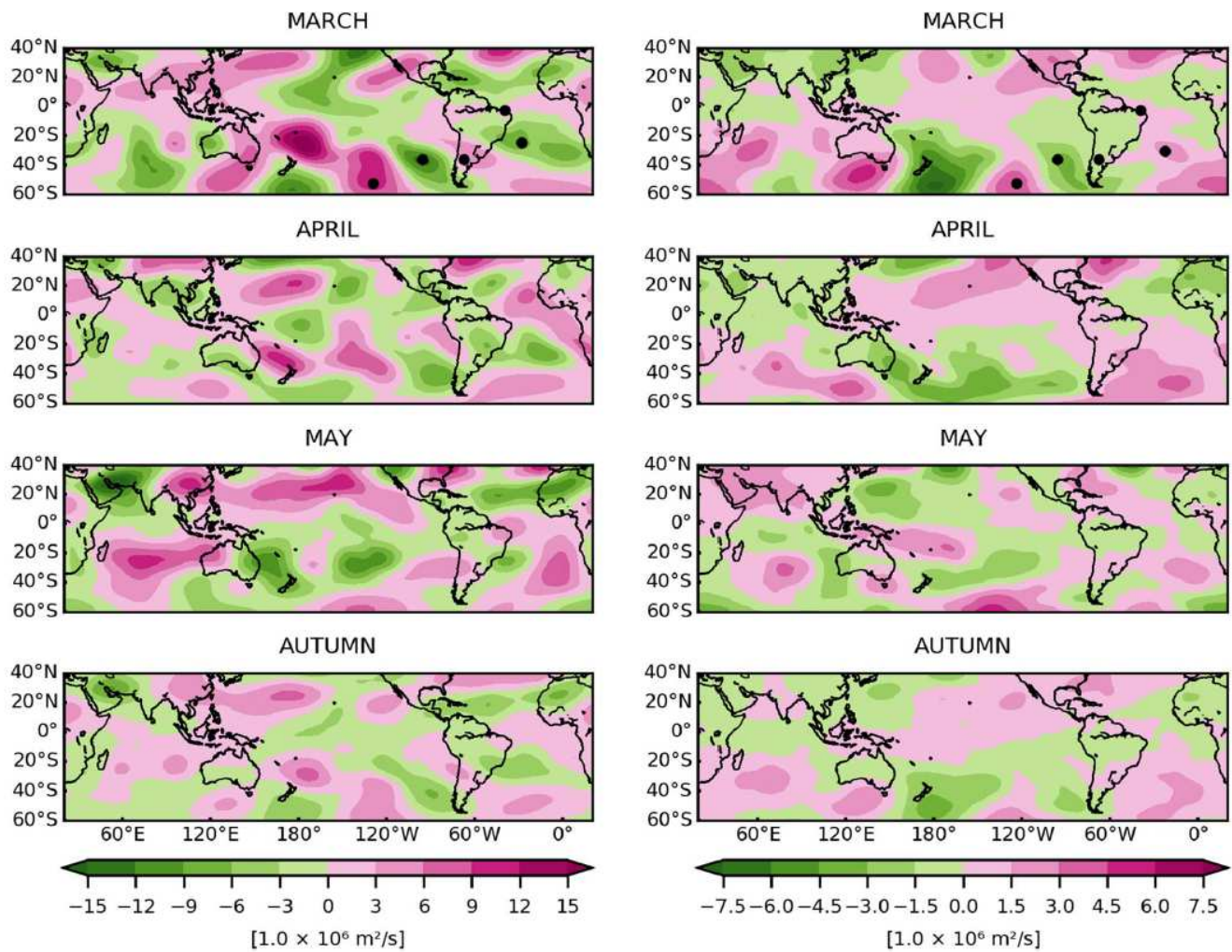


**Figure 6**

200-hPa (left panels) and 850-hPa (right panels) zonally asymmetric streamfunction (ZASTRF) anomalies for March, April, May, and autumn 2019. Black dots represent the target points 1–5 (from left to right), where circulation anomalies were assessed using the influence functions and LBM (please refer to Fig. 7 for additional details)

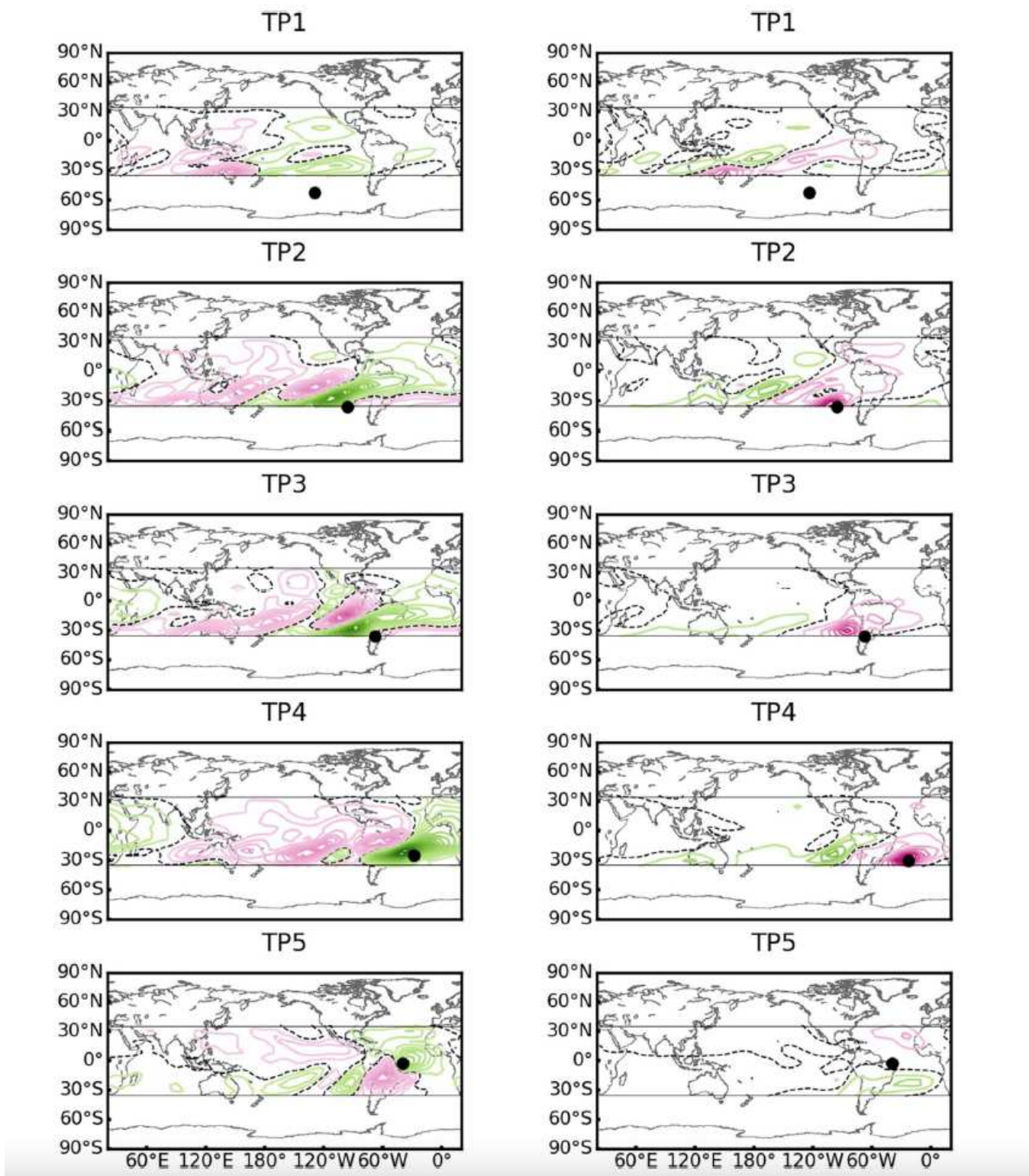


**Figure 7**

Influence functions results: 200-hPa (left panels) and 850-hPa (right panels) zonally asymmetric streamfunction (ZASTRF) anomalies for five target points (TP1–TP5 – black dots), considering the March climatological basic state. IFs were applied to modelled ZASTRF anomalies, between 35°S and 35°N (straight horizontal lines), on the 15th day of simulation. Magenta [green] contours ( $1 \times 10^6 \text{ m}^2/\text{s}$ )

indicate positive [negative] ZASTRF anomalies around the TP for positive diabatic heating anomalies. Dashed lines indicate the zero contour

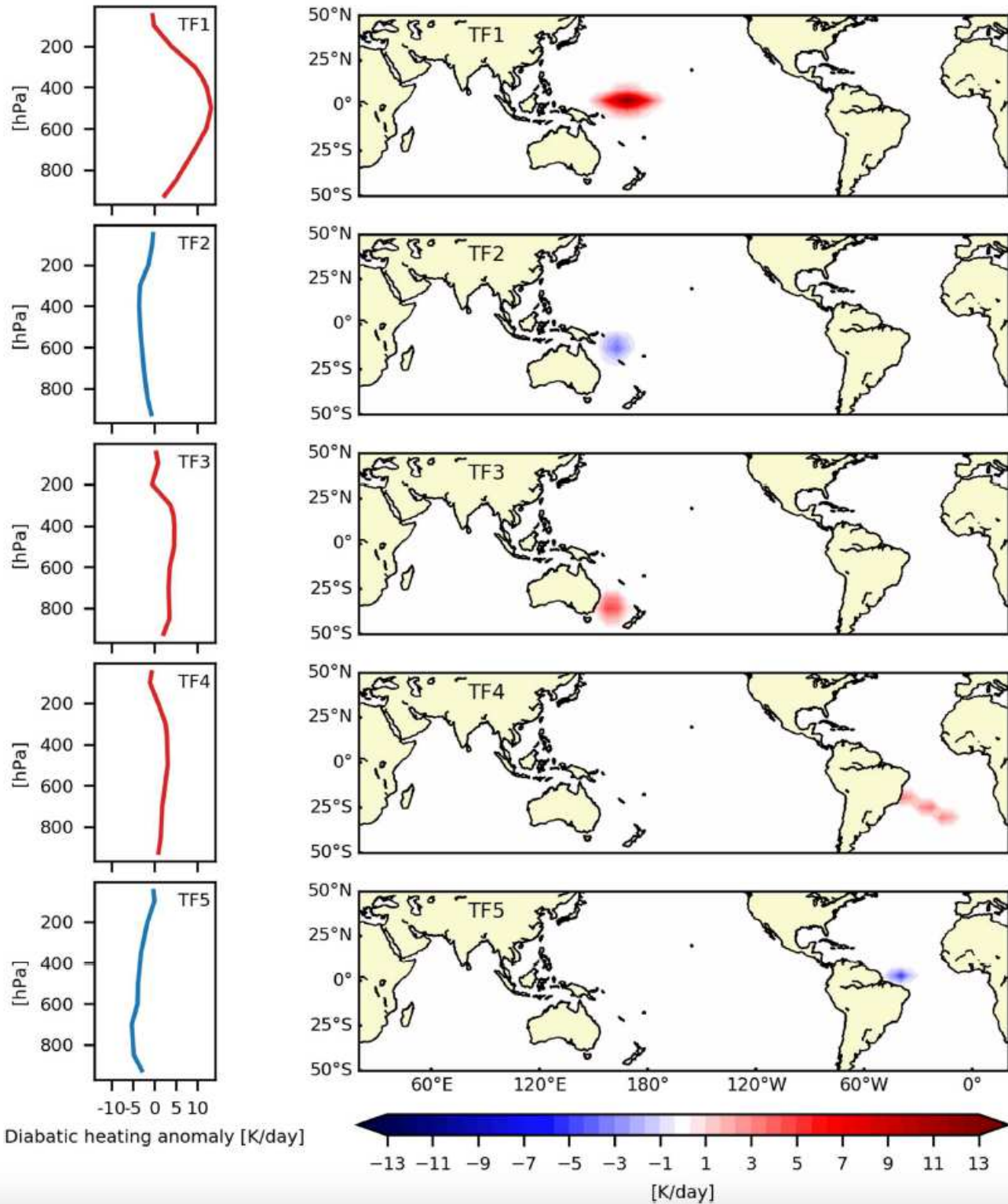
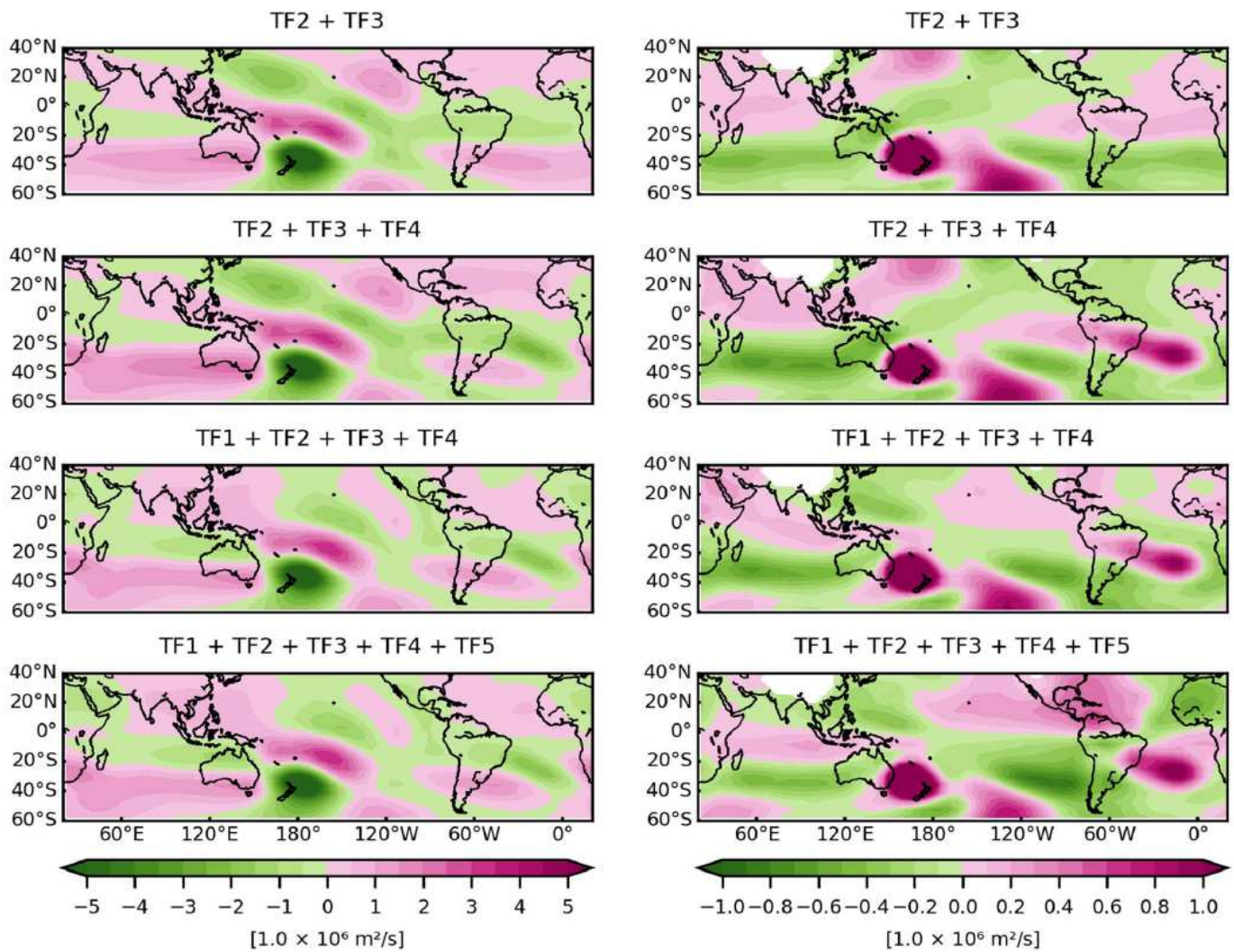


Figure 8

Vertical and horizontal distributions of the diabatic heating anomalies incorporated into the model's temperature tendency equation. TF stands for thermal forcing



**Figure 9**

Modelled 200-hPa (left panels) and 850-hPa (right panels) zonally asymmetric streamfunction (ZASTRF) results on the 15th day of simulation considering combinations among the thermal forcings (TFs) 1, 2, 3, 4, and 5

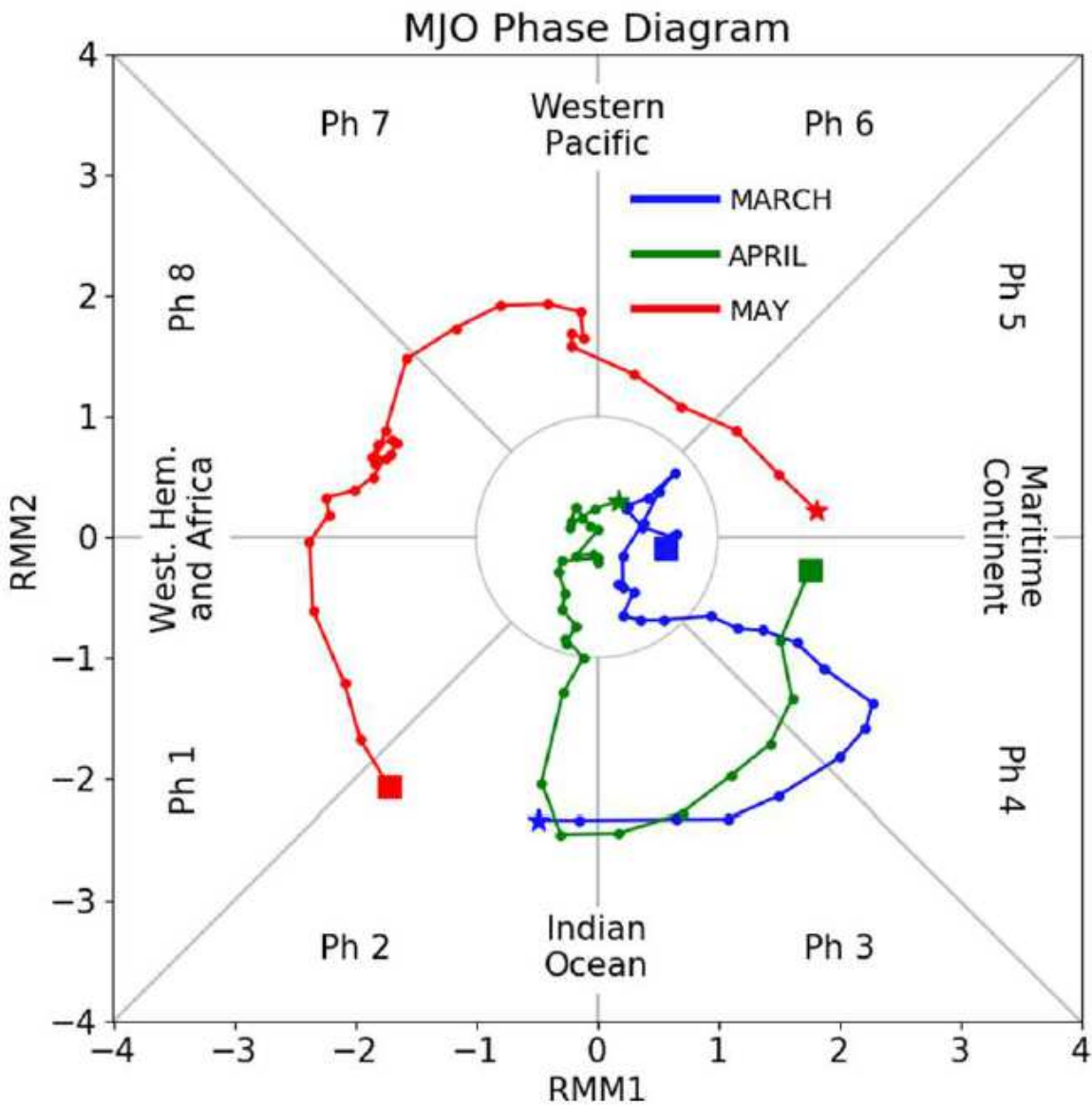


**Figure 10**

RMM diagram for March (blue), April (green), and May (red) 2019. Stars and squares represent the first and last days of the months, respectively. Full circles indicate the other days of the month, in ascending order, connected by straight lines. The central circle indicates an inactive MJO. Each region comprises the two MJO phases that are expected to enhance atmospheric convection over that region

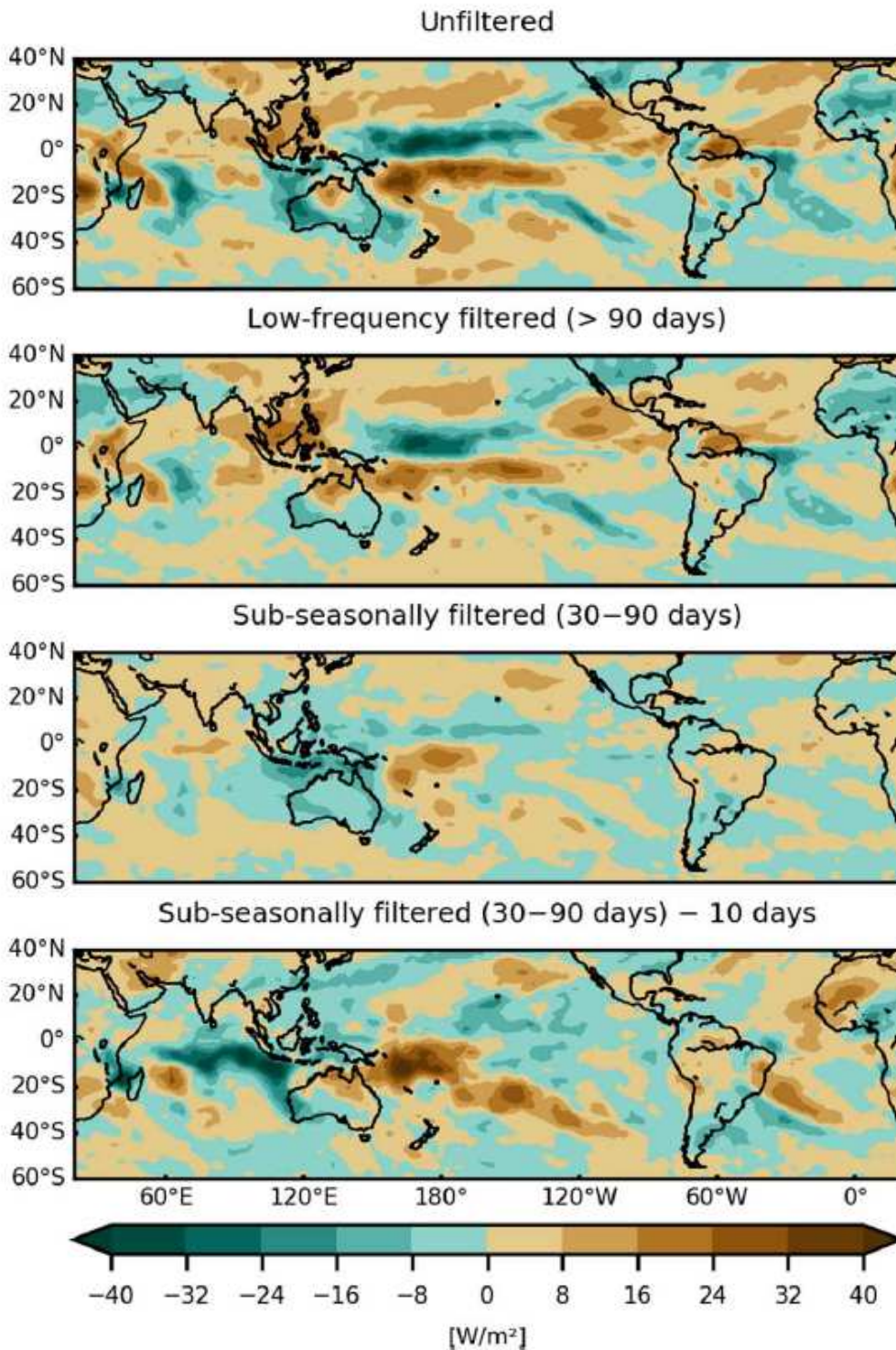


**Figure 11**

Mean outgoing longwave radiation (OLR) for March 2019: (upper panel) unfiltered; (upper-middle panel) low-frequency filtered (>90 days); (lower-middle panel) sub-seasonally filtered (30–90 days); and (lower panel) the first ten days of March 2019. Averages were calculated using daily OLR anomalies